Dynamic Si IGBT Model With Accurate Ringing Considering Time-Varying Bulk Resistance and Reverse Recovery Conductance

Yi Yu, Xuejun Pei, and Peng Zhou

***Abstract*—As the core of system electromagnetic interference (EMI) modeling in power electronics, the prediction of EMI sources requires high-precision switching device models. However, existing switching device behavioral models have limitations in characterizing the turn-ON and turn-OFF ringing effects of Si IGBT. To address the problem of poor ringing accuracy in existing models, a dynamic Si IGBT model is proposed, considering time-varying bulk resistance during turn-OFF and time-varying reverse recovery conductance during turn-ON. First, bulk resistance and reverse recovery conductance are identified as the dominant factors affecting turn-OFF and turn-ON ringing accuracy. Second, electrical parameters affecting bulk resistance and reverse recovery conductance are identified based on carrier distribution. Third, the dynamic bulk resistance and reverse recovery conductance are modeled based on the identified electrical parameters. Finally, the proposed dynamic Si IGBT model is validated through conducted EMI test, the results of which show that the ringing accuracy of EMI source and system EMI is improved by up to 19 and 17 dB, respectively.**

***Index Terms*—Bulk resistance, dynamic IGBT model, electromagnetic interference (EMI) source, reverse recovery conductance, ringing effect, system EMI.**

I. Introduction

IGBT-BASED power inverters are widely utilized in power generation and consumption systems due to their high efficiency and reliability. However, the electromagnetic interference (EMI) generated by these inverters is particularly severe, posing significant challenges to the reliable operation of surrounding electronic equipment [1]. To ensure compliance with stringent EMI emission standards [2], [3], power converters must undergo rigorous testing before market deployment. Consequently, research on EMI modeling has garnered substantial attention in both academia and industry [4].

Received 7 April 2025; revised 9 July 2025 and 12 August 2025; accepted 15 September 2025. Date of publication 17 September 2025; date of current version 13 November 2025. This work was supported in part by the National Natural Science Foundation of China under Grant 52377187 and in part by the China Postdoctoral Science Foundation under Grant 2024M761010. Recommended for publication by Associate Editor E. S. Lee. *(Corresponding author: Xuejun Pei.)*

The authors are with the State Key Laboratory of High Density Electrical Energy Conversion, Huazhong University of Science and Technology, Hubei 430074, China, and also with the School of Electrical and Electronic Engineering, Huazhong University of Science and Technology, Wuhan 430074, China (e-mail: d202180645@hust.edu.cn; ppei215@mail.hust.edu.cn; zhou_p@hust.edu.cn).

Color versions of one or more figures in this article are available at https://doi.org/10.1109/TPEL.2025.3611288.

Digital Object Identifier 10.1109/TPEL.2025.3611288

As the cornerstone of EMI emission modeling, accurate simulation and prediction of EMI sources is a critical challenge that must be addressed [6]. Currently, several methods for predicting EMI sources have been developed, primarily including: measurement-based model [5], [6], [8], [9], frequency domain envelope analytical model [10], [11], [12], time domain analytical model [13], [14], [15], [16], [17], [18], [19], [20], [21], [22], [23], and behavioral model [24], [25], [26], [27], [28], [29], [30], [31]. The comparisons of these method are summarized in Table I.

1) Measurement-based model: This model has high slope, ringing accuracy and can easily predict EMI source. However, the measurement-based model can only be developed after power electronic prototype has been assembled and are operating normally, which means the model is not a forward design method. Besides, the measurement-based model treats the total IGBT as black box without gate terminal, making it impossible to characterize the impact of drive parameters on EMI sources, and cannot provide guidance on how to adjust drive parameters to optimize EMI sources.
2) Frequency domain envelope analytical model based on fixed slope rate: This approach assumes that the slope of the waveform remains constant during switching transients and that the rise and fall times are identical across different operating conditions. It derives analytical expressions for the relationship between the envelope amplitude of the spectrum and waveform parameters such as rise and fall times. However, this method exhibits limited high-frequency accuracy, fails to account for ringing effects, and lacks topology universality. For instance, a model developed for a two-level inverter is not applicable to a three-level inverter [10].
3) Time domain analytical model based on waveform segmentation: This method segments the switching transient process into intervals based on device operating regions and solves piecewise state equations [19] or derives explicit solutions [17]. The slope accuracy is high, but ringing accuracy improvement has not been paid enough attention. Nevertheless, it also lacks topology universality, and users often need to modify the code to adapt to new devices or circuits.
4) Behavioral model based on software circuit component: The switching device behavioral model is constructed in

TABLE I
COMPARISONS OF EXISTING SWITCHING DEVICE MODELS FOR EMI SOURCE PREDICTION

Models	Ref	Slope Accuracy	Ringing Accuracy	Topology universality	No prototype needed
Dynamic Si IGBT behavior model	This paper	**High**	**High**	**Yes**	**Yes**
Measurement-based model	[5], [6]-[9], 2023	**High**	**High**	**Yes**	No
Frequency domain envelope analytical model	[10] [11] [12], 2024	Low	Low	No	**Yes**
Time domain analytical model	[13]-[23], 2024	**High**	Low	No	**Yes**
Behavioral model	[25]-[31], 2023	**High**	Normal	**Yes**	**Yes**

circuit simulation software using controlled sources to emulate nonlinear characteristics such as channel current [30] and interterminal capacitance [28], [29]. These models can be directly connected to external circuit components. Once developers complete the modeling and integrate it into the software library, users can directly employ the models in circuit simulations without needing to understand the internal principles, facilitating seamless adaptation to various power electronics topologies. Commercial software packages such as Simscape [32] and ANSYS [33] have also released characterization tools for switching device modeling, demonstrating the industry's recognition of this method. Therefore, prediction methods based on switching device behavioral models represent an efficient, high-accuracy, and user-friendly solution for EMI source simulation and prediction.

However, existing switching device models still face significant challenges in accurately predicting ringing phenomena. For instance, the SPICE models released by device manufacturers, which are typical behavioral models, often exhibit limited accuracy [28]. Moreover, SPICE models are unavailable for certain devices, such as the Infineon FS50R12KT4_B15 module [34] studied in this article. Additionally, most switching device models in the literature are data-sheet-driven, focusing on fitting static characteristics such as voltage-dependent interterminal capacitance, transfer characteristics, and output characteristics using various functions [26], [28], [29], [35], [36]. While these models capture static behavior, they fail to fully characterize the dynamic behavior of switching transients. Although the necessity of dynamic characteristics for model accuracy has been recognized in study [30], the existing study primarily focuses on SiC MOSFETs, which differ significantly in physical structure from IGBTs. Kundu and Sensarma [37] investigated the estimation of diode reverse recovery characteristics based on datasheet specifications but neglected the influence of voltage, current, and current slew rate on dynamic reverse recovery behavior. Consequently, this existing model lacks universal applicability across diverse operating conditions. Furthermore, piecewise linearization-based models cannot be directly integrated into more user-friendly behavioral models. The well-known Hefner model [24] is based on semiconductor physical parameters, it faces issues such as high model complexity and difficulty in obtaining parameters. Besides, since the Hefner model does not consider the field-stop layer of recent generation IGBT, it has low ringing accuracy. While Hao et al. [16], and Li et al. [26] considered the tail current during IGBT turn-OFF, they did not analyze turn-OFF ringing. More importantly, all these studies on switching device dynamic characteristics have not revealed the mechanisms by which dynamic behavior influences ringing, nor have they improved IGBT ringing modeling accuracy. As demonstrated in Section II, EMI source models primarily based on static characteristics exhibit ringing spectrum errors of up to 20 dB when compared to experimental results, which is terrible for EMI prediction. Therefore, there is an urgent need to develop a dynamic IGBT model capable of accurately predicting ringing phenomena.

TABLE II
DEFINITIONS OF CIRCUIT PARAMETERS IN THE PROPOSED MODEL

L_{BUS}	Busbar parasitic inductance	C_{CE}	C-E interterminal capacitance
R_{BUS}	Busbar parasitic resistance	C_{GE}	G-E interterminal capacitance
R_G	Driver resistance	C_{GC}	G-C interterminal capacitance
R_D	Diode forward resistance	C_{OSS}	Output capacitance of switching device
R_{CE}	IGBT C-E bulk resistance	Q_{rr}	Reverse recovery charge
I_L	Load current	Q_{free}	Charge released during reverse recovery
I_F	Diode forward current	k_{free}	Percentage of charge released
I_C	IGBT collector current	g_{rr}	Dynamic reverse recovery conductance
I_{IGBT}	IGBT current	F_S	Switching Frequency
$I_{IGBTsat}$	IGBT saturation current	v_{CE_PK}	Peak C-E Voltage of IGBT Ringing
I_{tail}	Tail current	v_{GE}	Gate-emitter voltage of IGBT
I_{ON}	Turn-on current	α	Damping coefficient of switching ringing
I_{OFF}	Turn-off current	i_{CEL}	Lower IGBT current
v_{CEL}	Lower IGBT voltage	v_{CEU}	Upper IGBT voltage

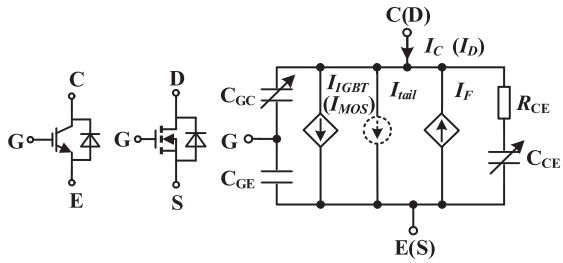

Fig. 1. Existing switching device behavioral model.

The existing switching device behavioral models are not applicable to the ringing dynamics of Si IGBT with errors up to 20 dB. This article proposes a novel dynamic IGBT model that incorporates time-varying bulk resistance during turn-OFF and time-varying reverse recovery conductance during turn-ON. The organization of this article is illustrated as follows. The parameters used in this article are defined in Table II. In Section II, existing switching device models as shown in Fig. 1 are reviewed and replicated. By comparing the experimental measurements with the simulation results of the existing model and the commercial model, it is shown that although the accuracy of the existing model is slightly higher than that of the commercial model, the ringing error is still as high as 20 dB. Then, the proposed dynamic IGBT model as shown in Fig. 2 is completed in Sections III and IV. Section III begins by deriving the equivalent circuit for turn-OFF ringing, proving that

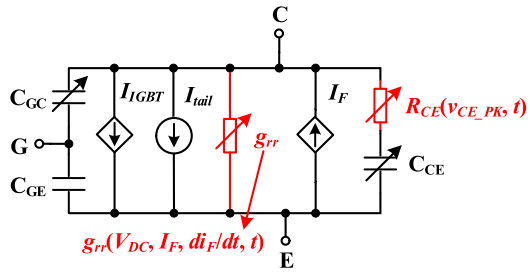

Fig. 2. Proposed dynamic Si IGBT model.

the tail current does not affect ringing damping. It identifies that the time-varying and voltage-dependent bulk resistance $R_{\rm CE}$, influenced by carrier distribution, significantly impacts ringing damping. A dynamic model for $R_{\rm CE}$, dependent on the ringing peak voltage $v_{\rm CE\_PK}$, is established, thereby improving turn-OFF ringing accuracy. Similarly, in Section IV, the strong damping effect of the freewheeling diode's reverse recovery conductance g_{rr} on ringing is identified, based on the equivalent circuit for turn-ON ringing. A time-varying reverse recovery conductance model is developed by experimentally extracting the relationship between g_{rr} and reverse recovery charge Q_{rr}, diode forward current I_F, current slew rate di_F/dt, and dc voltage $V_{\rm DC}$, enhancing turn-ON ringing accuracy. In Section V, the high ringing accuracy of the proposed model is validated under ten different operating conditions through double pulse test and conducted EMI test. Finally, Section VI concludes this article.

II. Limitations of Existing Switching Models in Characterizing Si IGBT Ringing Effects

In this section, the modeling methods and procedures of existing switching behavioral models are reviewed and replicated. The study focuses on the Infineon FS50R12KT4 module, which has a voltage–current rating of 1200 V/50 A. Then, the turn-ON and turn-OFF ringing waveforms and spectra of the existing model are shown, illustrating that the existing model still suffers from significant ringing errors.

A. Review and Replication of Existing Switching Behavioral Models

Fig. 1 depicts the existing switching device behavioral models, which primarily consist of voltage-dependent capacitors and controlled current sources. The gate–collector capacitance $C_{\rm GC}$ and collector–emitter capacitance $C_{\rm CE}$ are functions of the collector–emitter voltage $v_{\rm CE}$, while the gate–emitter capacitance $C_{\rm GE}$ can be considered constant. The channel current $i_{\rm ch}$ is composed of both the IGBT current $i_{\rm IGBT}$ and the diode current i_F. $i_{\rm IGBT}$ is influenced by both v_{GE} and v_{CE}, whereas i_F is affected by the diode forward voltage v_F, which is equivalent to $-v_{\rm CE}$. $R_{\rm CE}$ represents the semiconductor bulk resistance of IGBT or MOSFET. $i_{\rm tail}$ represents the tail current of IGBT.

First, the interterminal capacitances are extracted based on S parameters as detailed in Appendix A and modeled using (1). The parameters are listed in Table III, and a comparison of the fitted model and data is illustrated in Fig. 3(a). The method described in [19] is employed to determine the static

TABLE III
Model Parameters for FS50R12KT4 Si IGBT Module

Characteristics \ Parameters		a	b	c
$C_{CE}(v_{CE})$		2	3.6	0.3
$C_{GC}(v_{CE})$		1.2	3.8076	0.4423
IGBT transfer characteristic $i_{IGBTsat}(v_{GE})$		-0.1176	2.6750	
Diode forward characteristic $i_F(v_F)$		-5.2717	38.7073	
IGBT Output characteristic	$s_1(v_{GE})$	0.0077	-0.2532	2.5659
	$s_2(v_{GE})$	-0.0269	-1.0436	
	$s_3(v_{GE})$	-0.0053	0.1627	

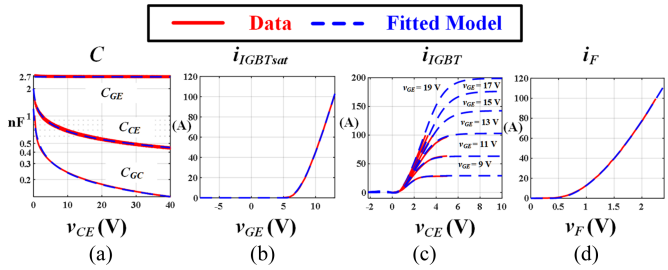

Fig. 3. FS50R12KT4 Si IGBT module static characteristic curve fitting results. (a) Interterminal capacitance. (b) Transfer characteristic. (c) Output characteristic. (d) Forward characteristic of diode.

$R_{\rm CE}$, yielding a value of 2 Ω

$$C = \frac{a}{(1 + bv_{\rm CE})^c}. \tag{1}$$

Second, the transfer characteristic $i_{\rm IGBTsat}\,(v_{\rm GE})$ is modeled using (2). $V_{\rm GEth} = 5.4$ V. The fitted parameters are placed in Table III, and a comparison of the data and the fitted model is shown in Fig. 3(b). Similarly, the forward characteristic of diode $i_F\,(v_F)$ shares the same fitting model (2). $V_{F\rm th} = 0.4$ V, and the fitted results are shown in Table III and Fig. 3(d).

Third, output characteristic $i_{\rm IGBT}\,(v_{\rm CE}, v_{\rm GE})$ should be modeled. However, the output characteristic curves in datasheets often provide only a limited range of parameters, which is insufficient for comprehensive modeling of $i_{\rm IGBT}\,(v_{\rm CE}, v_{\rm GE})$. Therefore, the modeling of output characteristics usually requires the help of transfer characteristics $i_{\rm IGBTsat}\,(v_{\rm GE})$. The output characteristic curve can be transformed into a univariate function modeling problem by simplifying it with the fixed $v_{\rm GE}$. The fitting process is as follows: For each $i_{\rm IGBT}(v_{\rm CE})$ curve in the output characteristic curve at a fixed $v_{\rm GE}$, the saturation current $i_{\rm IGBTsat}$ is first calculated using the already fitted model (2). Then, the output characteristic curve $i_{\rm IGBT}\,(v_{\rm CE})$ is fitted using (3) to obtain the parameters s_1, s_2, and s_3 for the current fixed $v_{\rm GE}$. This process is repeated for all $V_{\rm GE}$ values in the output characteristic curves, resulting in a series of $s_1(v_{\rm GE})$, $s_2(v_{\rm GE})$, and $s_3(v_{\rm GE})$ curves, which are subsequently fitted using (4), (5), and (6). All the parameters for this model are listed in Table III, and a comparison of the data and the fitted model is shown in Fig. 3(c)

$$i_{\rm IGBTsat}\,(v_{\rm GE}) = \begin{cases} a(v_{\rm GE} - v_{\rm GEth})^3 + b(v_{\rm GE} - v_{\rm GEth})^2, v_{\rm GE} \geq V_{\rm GEth} \\ 0, v_{\rm GE} < V_{\rm GEth} \end{cases} \tag{2}$$

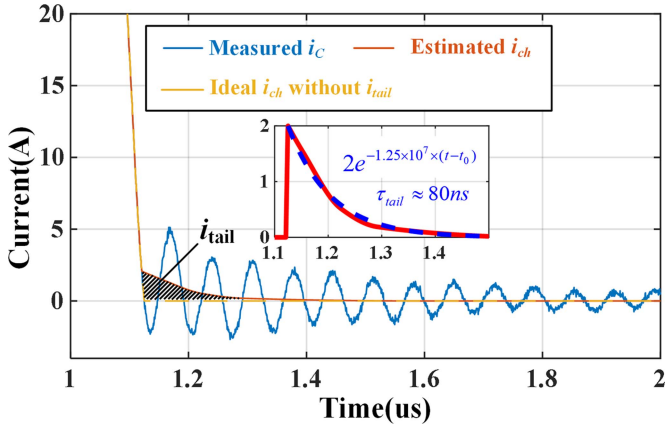

Fig. 4. Estimation of the tail current i_{tail}.

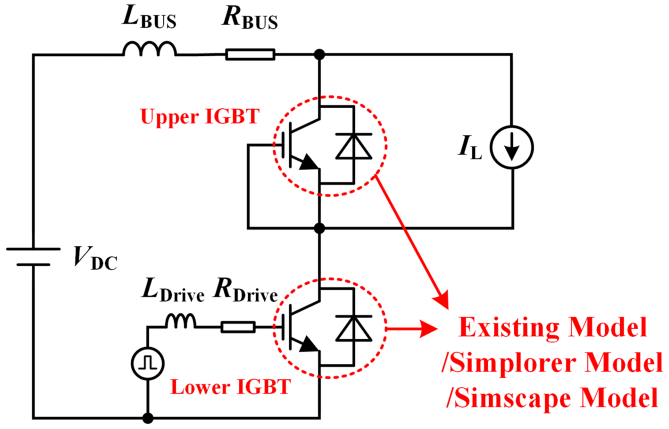

Fig. 5. Schematic of the double-pulse test circuit.

$$i_{\mathrm{IGBT}}(v_{\mathrm{GE}},v_{\mathrm{CE}}) = I_{\mathrm{IGBTsat}}\,(v_{\mathrm{GE}})\,[0.5\tan h(s_1\,(v_{\mathrm{GE}})\times v_{\mathrm{CE}} + s_2\,(v_{\mathrm{GE}})) + 0.5 - s_3\,(v_{\mathrm{GE}})\times e^{-(v_{\mathrm{CE}}-0.65)^2}] \quad (3)$$

$$s_1\,(v_{\mathrm{GE}}) = a{v_{\mathrm{GE}}}^2 + bv_{\mathrm{GE}} + c \quad (4)$$

$$s_2\,(v_{\mathrm{GE}}) = av_{\mathrm{GE}} + b \quad (5)$$

$$s_3\,(v_{\mathrm{GE}}) = av_{\mathrm{GE}} + b. \quad (6)$$

Finally, the tail current need to be modeled. The method described in study [27] is employed for tail current i_{tail} estimation. By connecting the midpoints of the ringing current, the ringing component can be approximately removed, allowing true i_{ch} to be derived. In the absence of i_{tail}, the ideal channel current would decrease rapidly to zero with an almost constant slope. Therefore, the shaded region in Fig. 4 represents i_{tail}, which can be accurately fitted using an exponential decay function, with a tail time of approximately 80 ns. Thanks to Infineon's field-stop IGBT technology, the tail current has been significantly reduced compared with IGBT without field-stop layer. Even ignoring the trailing current is reasonable.

B. Turn-Off Ringing Accuracy of the Existing Model

In the circuit simulation software, the existing switching device model shown in Fig. 1 is implemented, and the same parameters are used to construct the IGBT device model in commercial characterization tools, Simscape and ANSYS / Simplorer. Subsequently, a double-pulse test (DPT) circuit is built using the IGBT device models, as illustrated in Fig. 5.

The official simulation tool IPOSIM provided by Infineon can only generate macroscopic loss data and does not provide switching waveforms, making it unsuitable for predicting EMI source. Additionally, Infineon does not offer a SPICE model for this power module; instead, it provides a PLECS model. However, this PLECS model only includes turn-ON and turn-OFF losses and lacks essential components such as the channel current model and interterminal capacitance model. When imported into the Plexim / PLECS software, the simulation results essentially present an ideal switching device with instantaneous channel current transitions, which deviates significantly from experimental measurements. Therefore, this model is excluded from the following comparisons.

TABLE IV
SPECTRUM PROCESSING PARAMETERS

Standard	F_S	RBW	Detector	Duration
EN55032	20kHz	CE/RE: 9kHz/120kHz	Quasi Peak	20ms

For the following comparison, the ANSYS / Simplorer characterization tool and the MATLAB / Simscape IGBT model are selected as references. These commercial models and existing model are compared with experimental measurements to evaluate their accuracy in predicting IGBT behavior. The operating conditions for experimental validation are presented in Table V.

In Fig. 6 O1: (a) and (c), the waveforms during the lower IGBT turn-OFF are compared, including $v_{\mathrm{CE}L}$, $v_{\mathrm{CE}U}$, and $i_{\mathrm{CE}L}$. The results show that the ANSYS model exhibits poor accuracy, with significant deviations in the rising and falling edges compared to experimental measurements. This inaccuracy stems from the ANSYS model's failure to incorporate detailed interterminal capacitance curve parameters and its neglect of the voltage-dependent effects of the capacitance. The existing models from the literature and the Simscape model demonstrate excellent agreement with experimental measurements in both voltage and current waveforms. However, the Simscape model exhibits prolonged ringing without attenuation, which is attributed to the absence of the bulk resistance R_{CE} in its formulation. In contrast, the existing model, which includes R_{CE}, achieves higher accuracy in capturing the ringing behavior.

To simulate the EMI source waveforms of practical power electronic converters, the simulated and measured IGBT voltage waveforms of one complete pulse including rise and fall edges are repeated at a switching frequency of 20 kHz over a duration of 20 ms and processed using the quasi-peak (QP) algorithm of an EMI receiver [39], with the parameters listed in Table IV, in which CE represent conducted emissions and RE represent radiated emissions. The resulting QP voltage spectra for the upper and lower IGBTs are shown in Fig. 6 O1 (e) and (f). $v_{\mathrm{CE}L}$ spectrum characterizes turn-OFF ringing, while v_{CEU} spectrum characterizes turn-ON ringing.

In Fig. 6 O1: (e), the turn-OFF ringing spectra are compared. The Simscape model exhibits an excessively high ringing spectrum amplitude, exceeding the experimental results by 20 dB, due to the prolonged duration of its ringing waveform. In contrast, the existing model, which incorporates the bulk resistance

TABLE V
RINGING ACCURACY VALIDATION FOR EXISTING MODEL

Operating Condition	V_{DC}	I_{ON}	I_{OFF}	R_G	L_{BUS}	Simscape Model Error (turn-off, turn-on)	Existing Model Error (turn-off, turn-on)
O1	650 V	45 A	50 A	56 ohms	400 nH	(20 dB, 38 dB)	(5 dB, **15 dB**)
O2	650 V	20 A	20 A	56 ohms	400 nH	(34 dB, 39 dB)	(**20 dB, 17 dB**)

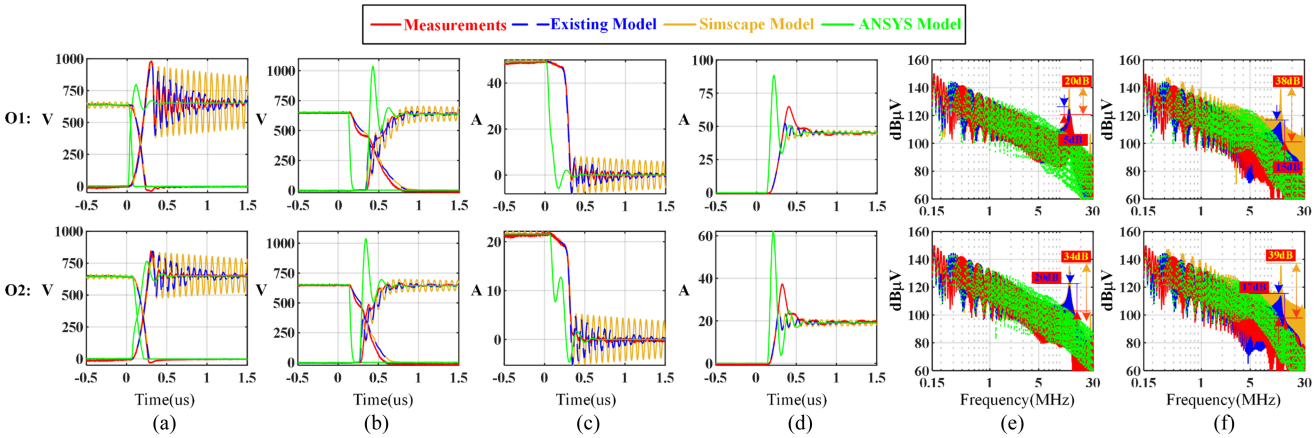

Fig. 6. Waveforms and QP spectra comparisons of measurements and different IGBT models at O1 and O2. (a) v_{CEL} and v_{CEU} during lower IGBT turn-OFF. (b) v_{CEL} and v_{CEU} during lower IGBT turn-ON. (c) i_{CEL} during lower IGBT turn-OFF. (d) i_{CEL} during lower IGBT turn-ON. (e) v_{CEL} spectrum characterizing turn-OFF ringing. (f) v_{CEU} spectrum characterizing turn-ON ringing.

R_{CE}, shows a smaller deviation of only 5 dB from the experimental spectrum. The ANSYS model, however, deviates from the experimental spectrum starting at 1 MHz, primarily due to inaccuracies in its rising and falling edge slopes.

However, the turn-OFF ringing accuracy of the existing literature model is not consistently reliable across all operating conditions. Fig. 6 O2: (a) and (c) illustrates the turn-OFF voltage and current waveforms under operating condition O2 with smaller load current. The results show that the experimentally measured ringing in v_{CEL} during turn-OFF decays significantly faster than that predicted by the existing model. Fig. 6 O2: (e) compares the QP spectra of the turn-OFF ringing v_{CEL}, processed using the parameters listed in Table IV. The existing model exhibits a significant deviation of 20 dB from the experimental measurements at the turn-OFF ringing. The turn-OFF ringing errors under different operating conditions are summarized in Table V. The ANSYS / Simplorer model error is not shown because its maximum error is not at the ringing frequency. These discrepancies highlight the limitations of the existing model in accurately capturing the ringing behavior under certain operating conditions, emphasizing the need for further refinement to improve its accuracy and applicability.

Therefore, the turn-OFF results demonstrate that the existing model achieves slightly higher accuracy compared to the commercial software models (ANSYS and Simscape). However, it still exhibits the turn-OFF ringing precision issues: While the lower IGBT ringing waveform shows high accuracy under heavy load conditions, its accuracy deteriorates significantly under light load conditions. The maximum deviation in the lower IGBT voltage ringing spectrum reaches 20 dB, indicating insufficient modeling of ringing dynamics across varying load conditions.

C. Turn-On Ringing Accuracy of the Existing Model

In Fig. 6 O1: (b) and (d), the waveforms during the lower IGBT turn-ON are compared, including v_{CEL}, v_{CEU}, and i_{CEL}. The v_{CEL} waveforms from the existing model, Simscape model, and experimental measurements are in close agreement. However, their upper IGBT voltage waveforms with turn-ON ringing show significant discrepancies. The large error in the ringing of the simulation models highlights the limitations of the existing model in accurately predicting the ringing behavior of the upper IGBT when the lower IGBT turns ON. Similarly, in Fig. 6 O2: (b) and (d), the waveforms during the lower IGBT turn-ON are compared at operating condition O2, including v_{CEL}, v_{CEU}, and i_{CEL}. The existing model still exhibits noticeable ringing, which deviates considerably from the experimental waveform.

In Fig. 6 O1: (f), the turn-ON ringing spectra are compared. the Simscape model's spectrum exceeds the experimental measurements by 38 dB, while the existing model also exceeds the measurements by 15 dB. These results indicate that the existing model achieves higher accuracy than Simscape model. However, it still exhibits significant errors in the upper IGBT voltage waveform during the lower IGBT turn-ON process, highlighting the need for further refinement in modeling techniques. In Fig. 6 O2: (f), QP spectra of turn-ON ringing at operating condition O2 are compared. The upper IGBT voltage waveform still exhibits anomalous ringing, which is absent in the experimental waveform. The maximum deviation in the upper IGBT voltage ringing spectrum is 17 dB, highlighting the model's inability to accurately predict the behavior of the upper IGBT during lower IGBT turns on. The turn-ON ringing errors under different operating conditions are summarized in Table V.

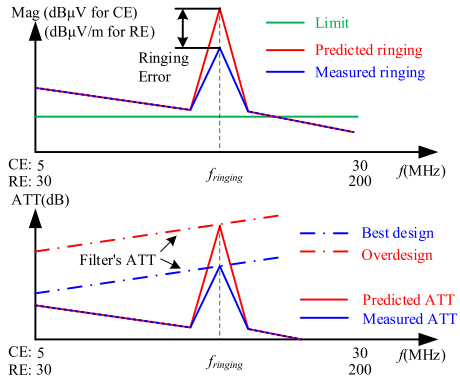

Fig. 7. Effects of ringing prediction errors on high frequency EMI filter design.

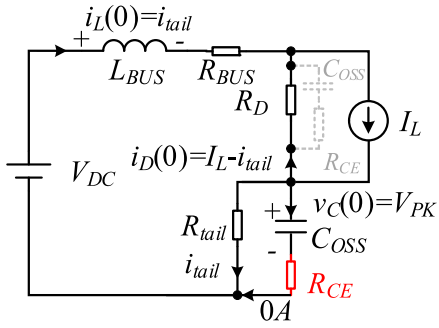

Fig. 8. Equivalent circuit for turn-OFF ringing process.

Therefore, under both light-load and heavy-load conditions, while the existing model demonstrates marginally higher accuracy in turn-ON ringing compared to commercial models, it still exhibits significant errors up to 17 dB.

D. Analysis of Ringing Effects on EMI

The ringing directly causes spikes in the CM and DM EMI source spectrum, which ultimately leads to spikes in the high-frequency CE EMI and RE EMI test results, and even causes the certification test to fail. Since the inductance of low-frequency filter inductors decreases significantly with frequency, high-frequency EMI at the 10 MHz level typically requires the additional design of NiZn based filter inductors [38]. And the design steps are shown in Fig. 7. DM and CM EMI magnitude with ringing are predicted and subtract the limit line to obtain the attenuation required for EMI filter. The design frequency band is about 5–30 MHz for high-frequency CE EMI and 30–200 MHz for RE EMI. The higher the attenuation curve of the filter, the larger the filter's parameters and the larger its volume. Therefore, as it can be seen in Fig. 7, whether it is high-frequency CE EMI or RE EMI filters, ringing prediction errors leads to significant overdesign, which is not beneficial to improving the power density of the product.

III. Dynamic Bulk Resistance Model for Turn-Off Ringing Accuracy Improvement

To improve the accuracy of turn-OFF ringing, the proposed model, as illustrated in Fig. 2, introduces dynamic bulk resistance R_{CE} ($v_{\mathrm{CE\_}PK}$, t). This following section systematically develops a turn-OFF ringing equivalent circuit that reveals the significant impact of R_{CE} ($v_{\mathrm{CE\_}PK}$, t) characteristics on ringing damping. The physical mechanisms governing R_{CE} are then analyzed in depth, through which key influencing parameters are identified. Finally, a universal dynamic bulk resistance model R_{CE} ($v_{\mathrm{CE\_}PK}$, t) applicable to multiple operating conditions is established, based on extensive experimental results.

A. Identification of Bulk Resistance As Dominant Factor Affecting Turn-Off Ringing Accuracy

The equivalent circuit depicted in Fig. 8 characterizes the ringing behavior during the final stage of the turn-OFF transition when the channel current has nearly diminished. The freewheeling diode connected in parallel with the upper IGBT conducts and can be equivalently modeled as a resistance R_D. The current of the upper diode has reached the load current. The resistance of the upper diode R_D is much smaller than the impedance of the parallel output capacitor C_{OSS}. The diode bypasses the C_{OSS}, so C_{OSS} of upper IGBT is ignored in the equivalent circuit. The tail current is modeled through resistance R_{tail}. The output capacitance C_{OSS} is initialized at its peak voltage state. The parasitic bus inductance L_{BUS} carries an initial current of i_{tail}. The circuit configuration constitutes a complete second-order state-response model. The system dynamics are governed by the second-order differential

$$\frac{d^2v_C}{dt^2}+\left(\frac{(R_{\mathrm{BUS}}+R_D+R_{\mathrm{CE}})R_{\mathrm{tail}}-R_{\mathrm{CE}}^2}{LR_{\mathrm{tail}}}\right)\frac{dv_C}{dt}\cdots +\left(\frac{R_{\mathrm{tail}}-R_{CE}}{LCR_{\mathrm{tail}}}\right)v_C=\frac{V_{\mathrm{DC}}+R_DI_L}{LC}. \tag{7}$$

The differential equation admits a general solution as given by (8), where the damping coefficient α and damped natural frequency ω_d are determined by circuit parameters in (10) and (11), while the phase angle θ and amplitude coefficient k depend on initial conditions in (13). Notably, since the tail current typically remains below 5 A, the equivalent resistance R_{tail} (on the order of hundreds of ohms) dominates over R_{CE}, R_D, and R_{BUS} by approximately two orders of magnitude. This significant disparity enables the simplification of α and ω_d by removing R_{tail}, as shown in (11) and (12). Crucially, this derivation demonstrates that the ringing damping coefficient α is independent of the tail current magnitude, but is fundamentally determined by the composite effects of R_{CE}, R_D, and R_{BUS}

$$v_C=V_S+ke^{-\alpha t}\sin(\omega_d t+\theta) \tag{8}$$

$$V_S=V_{\mathrm{DC}}+I_LR_D\approx V_{\mathrm{DC}} \tag{9}$$

$$\omega_d=\sqrt{\omega_0^2-\alpha^2} \tag{10}$$

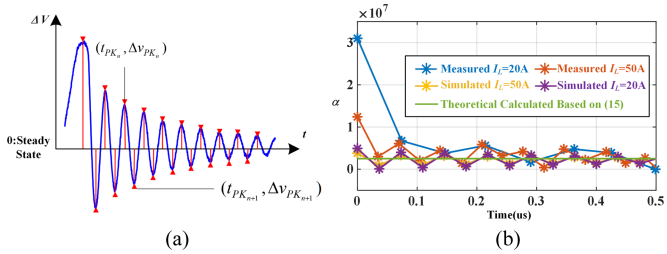

Fig. 9. Measured versus simulated turn-OFF damping coefficients α. (a) Experimental and simulation waveform processing methodology. (b) Comparative analysis of experimental results and theoretical calculations.

$$\alpha = \frac{(R_{\rm BUS} + R_D + R_{\rm CE})R_{\rm tail} - R_{\rm CE}^2}{2LR_{\rm tail}} \approx \frac{R_{\rm BUS} + R_D + R_{\rm CE}}{2L} \tag{11}$$

$$\omega_0 = \sqrt{\frac{R_{\rm tail} - R_{\rm CE}}{L_{\rm BUS}C_{oss}R_{\rm tail}}} \approx \sqrt{\frac{1}{L_{\rm BUS}C_{oss}}}. \tag{12}$$

Based on the initial voltage of the output capacitor $C_{\rm oss}$ and the initial current of the parasitic inductor $L_{\rm BUS}$, k, and θ can be calculated in (13).

The exponential term $ke^{-\alpha t}$ governs the decay characteristics of the ringing envelope, where the damping coefficient α remains nearly constant due to the combined effects of the diode's ON-state resistance R_D (0.04–0.1 Ω), fixed bus parasitic resistance $R_{\rm BUS}$, and constant bulk resistance $R_{\rm CE}$ in existing models, as mathematically established in (11). While the voltage-dependent variation of output capacitance $C_{\rm OSS}$ introduces minor perturbations to the natural frequency ω_0 and damped frequency ω_d as in (10), (12), their limited magnitude permits treating the amplitude coefficient k in (13) as a quasi-constant parameter, resulting in the simulated exponential decay profile of the ringing envelope $ke^{-\alpha t}$

$$\begin{cases} v_C(0) = v_{PK} \\ \frac{dv_C}{dt}\big|_0 = 0 \end{cases} \Rightarrow \begin{cases} V_{\rm DC} + k\sin(\theta) = v_{PK} \\ k(-\alpha\sin\theta + \omega_d\cos\theta) = 0 \end{cases}$$
$$\Rightarrow \begin{cases} \theta = \arctan\frac{\omega_d}{\alpha} \\ k = \frac{(v_{PK} - V_{\rm DC})\omega_0}{\omega_d} \end{cases}. \tag{13}$$

However, experimental measurements reveal significant deviations between the observed ringing envelope and the existing exponential decay model. Using the peak detection method illustrated in Fig. 9(a), the time-dependent damping coefficient $\alpha(t)$ is extracted through (8), (14), and (15), with calculation results presented in Fig. 9(b). While simulation waveforms (both $I_L = 50$ A and $I_L = 20$ A conditions) demonstrate nearly constant α values aligning with theoretical calculations, the experimental α in $I_L = 20$ A condition exhibits remarkable time-variation. The initial α value exceeds theoretical calculations by an order of magnitude before gradually decaying to theoretical levels. This dynamic damping behavior cannot be explained by existing models where $R_{\rm BUS}$ and $R_{\rm CE}$ are fixed parameters and R_D remains negligible

$$\Delta V = v_C - V_S \tag{14}$$

$$\alpha = -\frac{1}{t_{PK_{n+1}} - t_{PK_n}} \ln\left(\frac{\Delta v_{PK_{n+1}}}{\Delta v_{PK_n}}\right). \tag{15}$$

The analytical results from (11) demonstrate that the significant enhancement of the damping coefficient cannot be attributed to $R_{\rm tail}$ due to its inherently high impedance. Furthermore, the constant nature of $R_{\rm BUS}$ (determined by busbar and electrolytic capacitor parasitic) and the negligible contribution of R_D collectively indicate that the observed dynamic behavior must originate from the time-varying and load-dependent characteristics of bulk resistance R_{CE}. Notably, this phenomenon is uniquely observed in IGBTs (absent in MOSFETs [26], [30]), as confirmed by comparative switching waveform analysis. This distinct behavior necessitates a thorough investigation into the carrier dynamics governing $R_{\rm CE}$'s transient characteristics during IGBT turn-OFF, particularly focusing on minority carrier recombination processes and drift region extension effects in the bipolar conduction mechanism.

B. Identification of Peak Voltage as Dominant Factor Affecting Bulk Resistance

This article focuses on the Infineon FS50R12KT4 Si IGBT, a trench field-stop type device [34] featuring a specially designed field-stop layer [40] that effectively reduces tail current and minimizes turn-OFF losses. Fig. 10 presents a comprehensive co-analysis of the IGBT's turn-OFF ringing waveforms, carrier distribution, and equivalent circuit behavior under O1 and O2. In the figure, the red and blue circles represent hole and electron carriers, respectively; the superscript $+/-$ indicates relative doping concentrations; and the darker the color of the separated region, the greater the carrier concentration, the higher the conductivity, and the lower the resistance.

Under the operating condition O1: $V_{\rm DC} = 650$ V, and $I_L = 50$ A, the device exhibits pronounced ringing peaks and relatively low damping coefficients, with detailed waveform characteristics shown in Fig. 10(a).

The IGBT enters conduction when a positive gate voltage exceeding the threshold ($v_{\rm GE} > V_{\rm GEth}$) is applied, with its carrier distribution shown in Fig. 10(c). This conduction exhibits distinct bipolar transport characteristics: the gate voltage forms an inversion channel that injects electrons from the N^+ emitter into the N^- drift region, while simultaneously the P^+ collector injects holes into the same region under forward bias, creating bidirectional carrier transport with electrons drifting toward the collector and holes diffusing toward the emitter.

When a negative gate voltage is applied, the IGBT turns OFF and induces voltage ringing. Under this operating condition, the high load current and large current slew rate di_C/dt result in significant peak ringing voltage $v_{\rm CE\_PK}$. As illustrated in Fig. 10(d), the carrier distribution shows that the high blocking voltage rapidly sweeps out carriers from the N^- drift region, forming a depletion layer. The width of this depletion layer exhibits a direct correlation with the applied voltage v_{CE}. During the turn-OFF transient, the depletion layer expands dynamically, completely penetrating the lightly doped N^- drift region and extending into the N^+ field-stop layer. The depletion layer

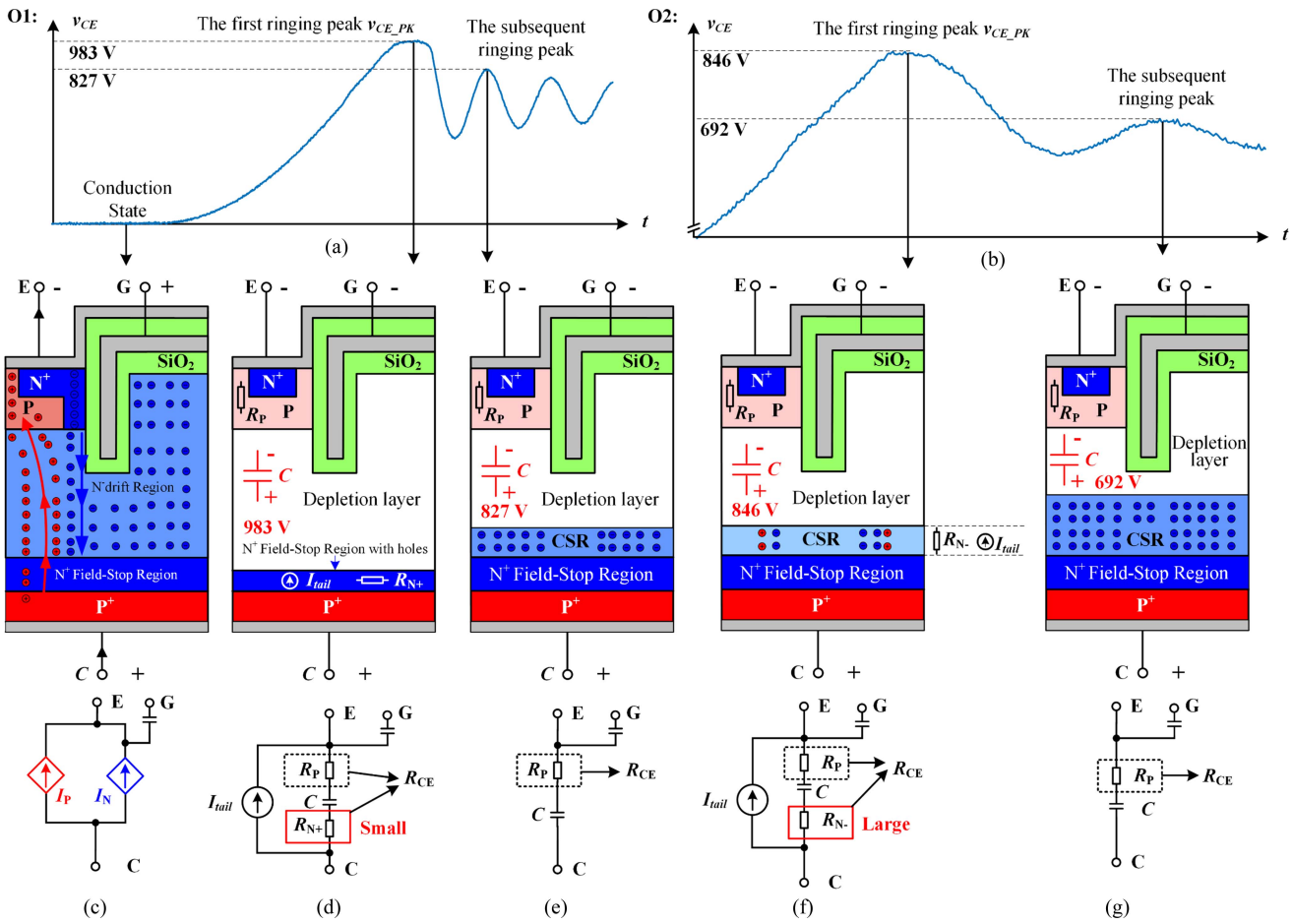

Fig. 10. Co-analysis of turn-OFF ringing characteristics, carrier distribution, and equivalent circuits for field-stop IGBT. (a), (b) Measured turn-OFF ringing waveform of O1 and O2. (c) Conduction state of O1. (d), (f) First ringing peak state of O1 and O2. (e), (g) Subsequent ringing peaks state of O1 and O2.

manifests as junction capacitance. Notably, the N^+ field-stop region maintains a high electron concentration, resulting in small residual hole density.

The conductivity of a semiconductor is revealed from (16) [41]. Where, σ is the conductivity of the semiconductor, which is inversely proportional to the resistivity. e is the fundamental charge unit, which is constant and does not vary with material and temperature. n is the number of free electrons per unit volume and p is the number of holes per unit volume. μ_n and μ_p are electron mobility and hole mobility, respectively, which characterize the average drift velocity of electrons and holes per unit electric field strength. μ_n is much larger than μ_p as shown in (17)

$$\sigma = e(n\mu_n + p\mu_p) \tag{16}$$

$$\mu_n \approx 3\mu_p. \tag{17}$$

In Fig. 10(d), the P^+ collector region, N^+ field-stop layer, and N^+ emitter region being heavily doped semiconductors, exhibit high conductivity and consequently low resistance. The series resistance R_{CE} of the IGBT's junction capacitance is primarily determined by the equivalent resistance R_P of the moderately doped P region. Furthermore, the recombination of few holes and electrons results in a slight reduction of carrier concentration in N^+ field-stop layer, i.e., decreases in both n and p in (16). Additionally, the mobility of holes μ_p is relatively low. These two factors collectively contribute to a slightly higher equivalent resistance R_{N+} during ringing compared to nonringing states, leading to a corresponding increase in R_{CE}.

When the IGBT voltage gradually decreases from the first peak of ringing, the carrier distribution is shown in Fig. 10(e). At this state, there are no remaining holes in the N^- drift region and the N^+ field stop region. As the voltage becomes smaller, the depletion layer becomes thinner. The collector injects a large number of electrons into the N^- drift region to thin the depletion layer, forming a carrier storage region (CSR) with high electron concentration, and the final depletion layer voltage is equal to the collector voltage. The carrier concentration is very high in all regions except the P region, the conductivity is very large, and the resistance is very small. The series resistance R_{CE} of the IGBT junction capacitance is mainly determined by the P region.

Fig. 10(b), (f), and (g) illustrates the correlation between turn-OFF ringing waveforms, carrier distributions, and equivalent circuits in a field-stop IGBT under operating condition O2: V_{DC} = 650 V and I_L = 20 A. Under this light-load condition with

small current slew rate, the peak voltage v_{CE_PK} is relatively low, as shown by the ringing waveforms in Fig. 10(b). Moreover, due to the small v_{CE_PK}, the depletion layer is relatively thin and fails to penetrate the entire lightly doped N-drift region in Fig. 10(f). The remaining N^- drift region, referred to as CSR, contains a number of holes and electrons at the beginning, and the two are recombined during the trailing current time, leading to a significant decrease in the carrier concentrations p and n of holes and electrons. In addition, the mobility of holes μ_p is relatively low. Based on (16), these two factors result in the equivalent resistance of the CSR being much larger than the static value, thus leads to significant increased R_{N^-} and R_{CE}. This causes the ringing's damping coefficient α to be larger, resulting in rapid ringing attenuation. Therefore, the fundamental reason for the increased damping coefficient α under light-load conditions is that the small ringing peak voltage V_{CE_PK} prevents the depletion layer from fully penetrating the N^- drift region, leaving the remaining CSR with a large number of holes. The holes and electrons are recombined leading to significantly decreased carrier concentrations p and n, ultimately leading to decreased σ, increased R_{N^-}, R_{CE} and larger damping coefficient α.

When the IGBT voltage decreases from the first ringing peak, the carrier distribution is shown in Fig. 10(g). As the IGBT withstand voltage decreases, the depletion layer shrinks, and the IGBT injects a large number of electrons from the external circuit into CSR through the collector. Due to the high electron concentration and large electron mobility, this region exhibits high conductivity and small equivalent resistance. R_{CE} is mainly determined by the resistance R_P of the moderately doped P region, and the equivalent resistance returns to its normal state. $R_{CE} = 2\ \Omega$.

In summary, the physical mechanism based on carrier distribution demonstrates that the lower the peak voltage of IGBT turn-OFF ringing, the thinner the depletion layer becomes, resulting in a thicker remaining CSR with low carrier concentrations and consequently increased R_{CE}. Therefore, R_{CE} exhibits negatively correlated with the ringing peak voltage v_{CE_PK}. R_{CE} is not directly related to load current, but rather because larger I_L produces higher di_C/dt and greater v_{CE_PK}, causing the bulk resistance R_{CE} at $I_L = 50$ A condition to be smaller than at $I_L = 20$ A condition. Furthermore, as the ringing voltage decreases, electrons are injected from the external circuit through the collector, increasing the carrier concentration in CSR and reducing its resistance, thus R_{CE} also displays time-varying characteristics. The above analysis applies to all types of Si IGBTs, regardless of whether they have trench gate or planar gate structures, as long as they have a field stop layer, they have dynamic R_{CE} characteristics.

C. Dynamic Bulk Resistance Modeling

The bulk resistance R_{CE} can only be solved indirectly through the damping coefficient α. The first damping coefficient α of the ringing in Fig. 9(b) is the key reason for the spectral error in the ringing model. By varying the load current I_L in double-pulse tests to change the peak voltage v_{CE_PK}, the damping coefficient α corresponding to different v_{CE_PK} values can be extracted.

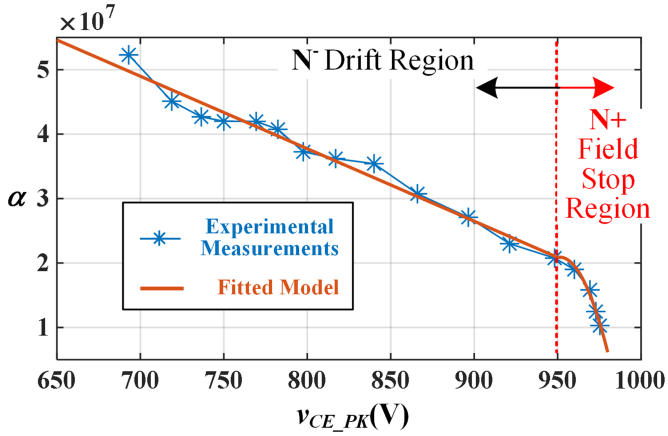

Fig. 11. Modeling α of versus v_{CE_PK}.

TABLE VI
PARAMETERS OF DYNAMIC R_{CE} MODEL

Parameters	p_1	p_2	p_3	p_4	τ_1	τ_2	k_R
Values	−1.12e5	2e7	−1.8e4	4.8e4	3e−9	55e−9	1.18e−6

Fig. 11 shows the curve of α versus v_{CE_PK}. When v_{CE_PK} is less than 950 V, α essentially exhibits a linear relationship with v_{CE_PK}. This is because v_{CE_PK} increases, the depletion layer thickens linearly, the CSR thins linearly, R_{CE} decreases linearly, and the damping coefficient α reduces linearly. When v_{CE_PK} exceeds 950 V, the depletion layer enters the N^+ field-stop region, causing R_{CE} to decrease significantly with the expansion of the depletion layer, and the damping coefficient α decreases markedly.

The dynamic bulk resistance R_{CE} explains why there is a significant discrepancy between simulated and experimental turn-OFF ringing waveforms at $I_L = 20$ A, while the waveforms match closely at $I_L = 50$ A. Under $I_L = 20$ A, the ringing peak voltage is relatively low at 800 V, resulting in a thick CSR containing holes, large R_{CE}, and consequently a large damping coefficient α. In contrast, at $I_L = 50$ A, the ringing peak voltage reaches 980 V, causing the depletion layer to penetrate into the N^+ field-stop region where electron concentration is high, leading to small R_{CE} and consequently a small damping coefficient α.

The damping coefficient α can be fitted using the piecewise function shown in (18), with parameters listed in Table VI. When $v_{CE\_PK} > 950$ V, a linear function is used for fitting; for v_{CE_PK} exceeding 950 V, a quadratic function shall be applied. The results of the fitted model and experimental measurements are presented in Fig. 11, demonstrating high accuracy

$$\alpha = \begin{cases} p_1\left(v_{CE\_PK} - 950\right) + p_2, v_{CE\_PK} \le 950\ \text{V} \\ p_3\left(v_{CE\_PK} - 950\right)^2 + p_4\left(v_{CE\_PK} - 950\right) + p_2 \\ v_{CE\_PK} > 950\ \text{V} \end{cases}, . \tag{18}$$

Since (11) is derived under the condition that both α and R_{CE} are time-invariant parameters, its variant form $R_{CE} \approx$

$2L\alpha = 8\text{e-}7\alpha$ cannot be directly used to calculate R_{CE}, as the proportionality coefficient may deviate from 8e-7. Moreover, it is inappropriate to approximate the bulk resistance as abruptly changing from static value 2 ohms to a dynamic value after the ringing peak and then back to 2 Ω after a certain duration, as such discontinuous resistance would introduce artificial nonsmoothness in the voltage waveform.

Given that the bulk resistance rapidly emerges due to channel turn-OFF and quickly diminishes through external electron extraction, its transient behavior can be effectively modeled by a Gaussian function as shown in (19) and (20). The parameter $\tau_1 = 3$ ns characterizes the rapid resistance buildup. When the ringing voltage reaches its trough and begins to rise, large electrons have been injected into the CSR, thus the resistance R_{CE} recovers to 2 Ω with $\tau_2 = 55$ ns. The peak resistance $R_{\mathrm{CE\_}PK}$ correlates with the initial damping coefficient α as expressed in (21). The proportionality constant k_R between $R_{\mathrm{CE\_}PK}$ and α, determined through simulation-experimental waveform fitting, equals 1.18e-6, which is slightly larger than the 8e-7 estimate from (11) for time-invariant parameters, owing to the resistance decay process

$$R_{\mathrm{CE}} = R_{\mathrm{CE\_}PK}\left(\alpha\left(v_{\mathrm{CE\_}PK}\right)\right) \times e^{-\left(\frac{t-t_{PK}}{\tau}\right)^2} + 2 \tag{19}$$

$$\tau = \begin{cases} \tau_1, t < t_{PK} \\ \tau_2, t > t_{PK} \end{cases} \tag{20}$$

$$R_{\mathrm{CE\_}PK} = k_R \alpha. \tag{21}$$

To implement the time-varying bulk resistance into the IGBT behavioral model, the following three functions must be achieved:.

1) Turn-OFF caused by v_{GE} reduction is detected.
2) The moment when v_{CE} reaches its peak is detected.
3) Refresh t_{PK}, $v_{\mathrm{CE\_}PK}$ and calculate the dynamic bulk resistance R_{CE} based on (18)–(21).

These functions require a flag-based detection algorithm. The simplified pseudocode in Algorithm 1 can be deployed in the behavioral model. To ensure accurate ringing peak detection, the v_{CE} rising-edge threshold V_{CEth} is typically set to 50 V, and the v_{GE} falling-edge threshold V_{GEth} is set to 3 V.

Algorithm 1: Dynamic Bulk Resistance Refresh and Calculation Logic.

Input:
RiseFlagB // Rising-edge flag from previous timestep
$\boldsymbol{v_{CEB}}$, $\boldsymbol{v_{CE}}$ // Collector-emitter voltage (previous, current)
$\boldsymbol{v_{GE}}$ // Gate-emitter voltage
$\boldsymbol{dv_{CE}dtB}$, $\boldsymbol{dv_{CE}dt}$ // $\boldsymbol{v_{CE}}$ time derivative (previous, current)
$\boldsymbol{t}$ // Current simulation time
$\boldsymbol{t_{PKB}}$ // Peak time variable from previous R_{CE} calculation
$\boldsymbol{v_{CE\_PKB}}$ // Previous peak v_{CE}

Output:
$\boldsymbol{R_{CE}}$ // Bulk resistance
RiseFlag // Rising-edge detection flag
$\boldsymbol{v_{CE\_PK}}$ // Peak V_{CE} of this turn off process

1. If $\boldsymbol{v_{CE}} > V_{CEth}$ AND $\boldsymbol{v_{CEB}} < V_{CEth}$ AND $\boldsymbol{v_{GE}} > V_{GEth}$
   – IGBT is turning off
   – Set ***RiseFlag*** $= 1$
   Else
   – ***RiseFlag*** $=$ ***RiseFlagB***. End.

2. If $\boldsymbol{dv_{CE}dtB} > 0$ AND $\boldsymbol{dv_{CE}dt} < 0$ AND ***RiseFlag*** $== 1$
   – First ringing peak detected
   – Set ***PeakFlag*** $= 1$
   – Reset ***RiseFlag*** $= 0$
   Else
   – ***PeakFlag*** $= 0$. End.

3. If ***PeakFlag*** $== 1$
   – Refresh the dynamic bulk resistance parameters
   – Set $\boldsymbol{v_{CE\_PK}} = \boldsymbol{v_{CE}}$, $\boldsymbol{t_{PK}} = \boldsymbol{t} + 10$ ns
   Else Use previous dynamic bulk resistance parameters
   – Set $\boldsymbol{v_{CE\_PK}} = \boldsymbol{v_{CE\_PKB}}$, $\boldsymbol{t_{PK}} = \boldsymbol{t_{PKB}}$. End.
   Calculate R_{CE} using (18)–(21)

IV. Dynamic Reverse Recovery Conductance Model for Turn-On Ringing Accuracy Improvement

To improve the accuracy of turn-ON ringing, the proposed model, as illustrated in Fig. 2 introduces dynamic reverse recovery conductance g_{rr} (V_{DC}, I_F, di_F/dt, t). The following section systematically develops a turn-ON ringing equivalent circuit that reveals the significant impact of g_{rr} characteristics on ringing damping. The physical mechanisms governing g_{rr} and reverse recovery charge Q_{rr} dynamics are then analyzed in depth, through which key influencing parameters are identified. Finally, a universal dynamic reverse recovery conductance model g_{rr} (V_{DC}, I_F, di_F/dt, t) applicable to multiple operating conditions is established, based on extensive experimental results.

A. Identification of Reverse Recovery Conductance as Dominant Factor Affecting Turn-On Ringing Accuracy

As first stated in study [13], there are two cases of turn-ON transient. Fig. 12 illustrates two equivalent circuits for turn-ON ringing. The developed equivalent circuits accurately represent the turn-ON switching transient with the following initial conditions: 1) upper diode current decaying to zero while IGBT current and parasitic inductor current reach load current I_L; 2) upper device output capacitance voltage initialized at 0 V.

When L_{BUS} and the slew rate of $i_{\mathrm{CE}L}$ are both large, the initial $v_{\mathrm{CE}L}$ is nearly 0 and the lower IGBT is completely in the on-state. The ON-state resistance R_{ON} bypasses C_{OSS}, so C_{OSS} at lower IGBT is ignored in the case I circuit as shown in Fig. 12(a). The circuit topology models the upper IGBT as output capacitances with static bulk resistance

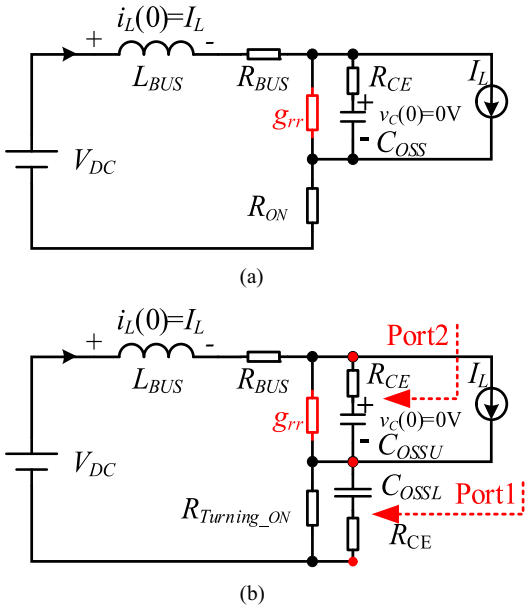

Fig. 12. Equivalent circuits for turn-ON ringing process. (a) Case I: IGBT works in ohmic region. (b) Case II: IGBT works in the saturation region.

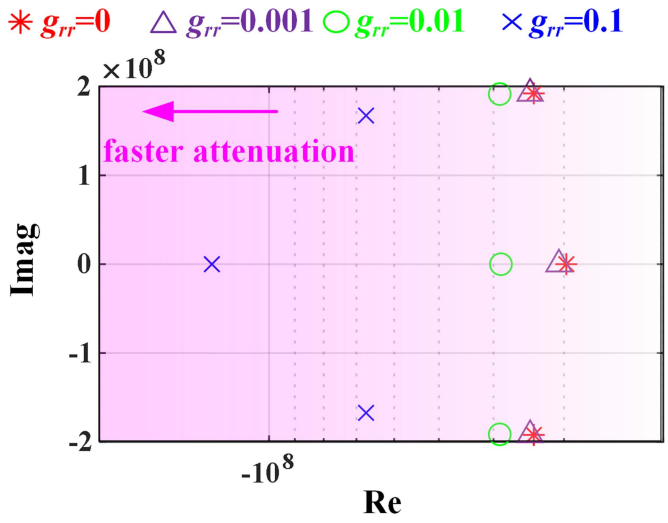

Fig. 13. Distribution of the poles for case II turn-ON ringing, where $R_{\mathrm{BUS}} = 0.21\ \Omega$, $R_{CE} = 2\ \Omega$, $L_{\mathrm{BUS}} = 100$ nH, $C_{\mathrm{OSSU}} = 500$ pF, $C_{\mathrm{OSSL}} = 300$ pF, $R_{\mathrm{Turning\_ON}} = 100\ \Omega$.

R_{CE}, incorporates diode reverse recovery effects through parallel conductance g_{rr}. The bulk resistance R_{CE} is modeled as a constant parameter under the upper IGBT's OFF-state condition. This configuration establishes a complete second-order circuit state-response model, with the system dynamics governed by the differential (22) shown at the bottom of this page, that precisely describes the resonant interaction between circuit parasitic during the critical turn-ON transition period.

This equation has a form similar to (7), so that the expression for the attenuation coefficient α can be calculated as in (23) shown at the bottom of this page. The number of output capacitance C_{OSS} (pF, 10^{-12} F) is always much smaller than that of bus parasitic inductance L_{BUS} (nH, 10^{-9} H). Therefore, the first and third item can be ignored. And α is simplified to (24) shown at the bottom of this page. This formulation (24) reveals that the reverse recovery conductance g_{rr} and C_{OSS} plays a dominant role in switching waveform damping characteristics. Besides, C_{OSS} has already been taken into account in existing models. Therefore, g_{rr} should be the reason causing turn-ON ringing prediction error for case I. The larger g_{rr} becomes, the stronger the damping effect and the weaker the resulting voltage ringing

$$\alpha \approx \frac{1}{2C_{oss}\left(\frac{1}{g_{rr}} + R_{\mathrm{CE}}\right)} \Rightarrow g_{rr} \uparrow \alpha \uparrow . \tag{24}$$

When L_{BUS} and the slew rate of $i_{\mathrm{CE}L}$ are both small, the initial $v_{\mathrm{CE}L}$ is nearly V_{DC} and the lower IGBT is still in the saturation region. The equivalent resistance $R_{\mathrm{Turning\text{-}ON}} = v_{\mathrm{CE}L}/i_{\mathrm{CE}L}$ is even several hundred ohms and cannot bypasses C_{OSS}, so C_{OSS} at lower IGBT cannot be ignored in the case II circuit as shown in Fig. 12(b). It is difficult to calculate the parsing solution of the attenuation coefficient for the third-order circuit. Therefore, the poles analysis method in study [42] is adopted. The two ports network is show in Fig. 12(b). Port 1 and Port 2 corresponds to $v_{\mathrm{CE}L}$ and $v_{\mathrm{CE}U}$, respectively. The real and imaginary parts of the two-port network poles reflect attenuation rate and the oscillation frequency, respectively. An example of poles distribution and corresponding parameters are shown in Fig. 13. The smaller the real parts of the poles, the faster the oscillation decays. As g_{rr} increases, the real part of the pole decreases. Therefore, Fig. 13 shows adding g_{rr} accelerates the decay of the oscillation.

$$\frac{d^2 v_C}{dt^2} + \frac{C_{oss}\left(R_{\mathrm{CE}} + R_{\mathrm{BUS}} + R_{\mathrm{ON}}\right) + \left(L_{\mathrm{BUS}} + \left(R_{\mathrm{BUS}} + R_{\mathrm{ON}}\right) C_{oss} R_{\mathrm{CE}}\right) g_{rr}}{L_{BUS} C_{oss}\left(1 + g_{rr} R_{CE}\right)} \frac{dv_C}{dt} \cdots + \frac{1 + g_{rr}\left(R_{\mathrm{BUS}} + R_{\mathrm{ON}}\right)}{L_{\mathrm{BUS}} C_{oss}\left(1 + g_{rr} R_{\mathrm{CE}}\right)} v_C = \frac{V_{\mathrm{DC}} - I_L\left(R_{\mathrm{BUS}} + R_{\mathrm{ON}}\right)}{L_{\mathrm{BUS}} C_{oss}\left(1 + g_{rr} R_{\mathrm{CE}}\right)}. \tag{22}$$

$$\alpha = \frac{\overbrace{C_{oss}\left(R_{\mathrm{CE}} + R_{\mathrm{BUS}} + R_{\mathrm{ON}}\right)}^{\text{first item}} + \overbrace{L_{\mathrm{BUS}} g_{rr}}^{\text{second item}} + \overbrace{\left(R_{\mathrm{BUS}} + R_{\mathrm{ON}}\right) C_{oss} R_{\mathrm{CE}} g_{rr}}^{\text{third item}}}{2 L_{\mathrm{BUS}} C_{oss}\left(1 + g_{rr} R_{\mathrm{CE}}\right)}. \tag{23}$$

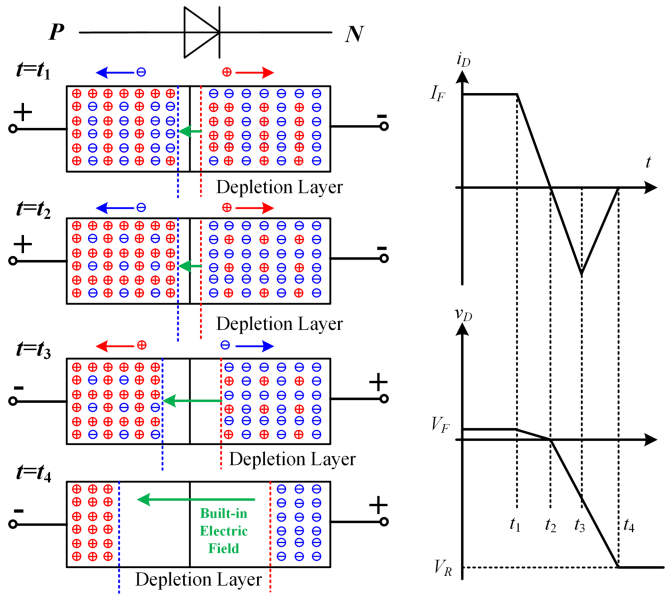

Fig. 14. Co-analysis of carrier distribution and external characteristics during diode reverse recovery. (a) Carrier distribution and movement. (b) Simplified external characteristic curve.

In summary, regardless of whether it is case I or case II, developing an accurate model for g_{rr} is critical for achieving precise simulation of turn-ON voltage ringing waveforms.

B. Identification of V_{DC}, I_F, *and* di_F/dt *as Dominant Factors Affecting Reverse Recovery Conductance*

In order to establish a dynamic characteristic model of reverse recovery with multioperating condition universality, it is first necessary to reveal the physical mechanism of the reverse recovery characteristics and clarify the influencing factors of reverse recovery.

The carrier distribution and motion at different states of the diode reverse recovery process are shown in Fig. 14, and the stationary lattice in the depletion layer is neglected in Fig. 14(a). Fig. 14(b) shows the simplified external characteristic curve of the diode reverse recovery process.

At $t = t_1$, the diode operates in forward conduction mode where electrons from the N region traverse the depletion layer into the P region under the applied electric field, while holes from the P region diffuse in the opposite direction, collectively establishing the forward current I_F. The greater the forward current I_F, the more electrons exist in the P region and the more holes exist in the N region.

At $t = t_2$, the diode operates in a critical conduction state where it ceases current output, yet retains residual minority carriers, specifically electrons in the P region and holes in the N region. These remaining charge carriers, collectively termed minority carriers, form the fundamental source of reverse recovery charge. Importantly, the concentration of minority carriers exhibits a direct correlation with the current decay rate (di_F/dt) during the t_1-t_2 interval: a steeper current fall slope results in proportionally greater residual minority carrier concentration.

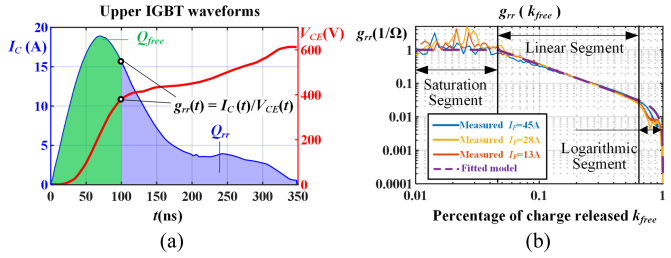

Fig. 15. Modeling of reverse recovery conductance influenced by reverse recovery charge. (a) Calculation methodology for conductance g_{rr} versus released charge percentage k_{free}. (b) Experimentally derived g_{rr} versus k_{free} characteristics from multiple operating conditions.

At $t = t_3$, the diode enters reverse bias operation, causing carriers to be swept out by the electric field, which progressively widens the depletion region. The resulting space-charge potential partially offsets the applied reverse voltage V_{DC}, with the removed carriers constituting the reverse recovery current.

At $t = t_4$, the diode reaches complete cutoff state where an extended depletion region forms to counterbalance the applied high reverse voltage. And the higher the withstand voltage V_{DC}, the thicker the depletion layer, the more carriers are discharged, and the greater the reverse recovery charge.

Therefore, the reverse recovery charge is influenced by three key parameters: the reverse dc voltage V_{DC}, forward current I_F, and current slew rate di_F/dt, all of which must be considered in the dynamic modeling process. Furthermore, the reverse recovery conductance and charge concentration are positively correlated.

C. Dynamic Reverse Recovery Conductance Modeling

Due to the small output capacitance in upper IGBT and diode, both its stored charge and displacement current are insignificant compared to those through the conductance g_{rr}, allowing the approximation that the reverse recovery current equals the current through g_{rr}. The time-varying g_{rr} (t) can be obtained by extracting the ratio of current to voltage in the transient waveform, after the current and voltage are denoised by the wavelet denoiser in MATLAB [43].

However, merely characterizing the time-varying g_{rr} during a single reverse recovery event fails to establish a universal g_{rr} model applicable across diverse operating conditions. The fundamental mechanism governing reverse recovery conductance stems from the residual carriers in silicon-based diodes, as these stored carriers are gradually swept out during the reverse recovery process, the conductance correspondingly decays. This physical understanding necessitates establishing the intrinsic relationship between g_{rr} and swept out charge Q_{free} as the primary modeling approach.

Fig. 15(a) presents the reverse recovery current and voltage waveforms under conditions of $V_{\text{DC}} = 650$ V and $I_L = 45$ A. For any instant during this process, the following three key parameters can be determined:

1) the instantaneous conductance $g_{rr}(t)$;
2) the released charge Q_{free} (indicated by the green shaded area in the figure) calculated using (25);

TABLE VII
PARAMETERS OF DYNAMIC $G_{\rm rr}$ MODEL

a	b	c	d	p_1	p_0
0.3	−0.0337	−1.3187	−1.5	0.0013	0.1553
p_{00}	p_{10}	p_{01}	p_{20}	p_{11}	p_{02}
0.0435	0.0396	1.5775	−0.0002	0.0065	0.2584

3) the total reverse recovery charge Q_{rr} (represented by the purple shaded area in the figure) obtained through (26).

The percentage of released charge $k_{\rm free}$ at each moment can then be derived according to (27). When plotting the $k_{\rm free}$ versus g_{rr} curves obtained from various operating conditions in Fig. 15(b), all curves demonstrate identical characteristics. Notably, while different load currents produce varying Q_{rr} values, the same functional relationship between $k_{\rm free}$ and g_{rr} is maintained. This observation confirms the model's universal applicability, as its validity remains unaffected by changes in the operating conditions

$$Q_{\rm free}(t) = \int_0^t I_{rr}(t)\,dt \tag{25}$$

$$Q_{rr} = \int_0^{t_{rr}} I_{rr}(t)dt \tag{26}$$

$$k_{\rm free}(t) = Q_{\rm free}(t)/Q_{rr}. \tag{27}$$

The reverse recovery conductance g_{rr} and released charge percentage $k_{\rm free}$ exhibit variations across an extensive dynamic range, necessitating a double logarithmic domain fitting approach to ensure modeling precision. The implemented three-segment model demonstrates distinct characteristics.

1) When $\log_{10}(k_{\rm free}) > -0.2$, that is, $k_{\rm free} > 0.63$, indicating small residual charge, $\log_{10}(g_{rr})$ decreases dramatically with $\log_{10}(k_{free})$, and g_{rr} approaches 0 at complete release. This segment is accordingly modeled using a logarithmic function.
2) When $\log_{10}(k_{\rm free}) < -0.2$, $\log_{10}(g_{rr})$ decreases linearly with $\log_{10}(k_{\rm free})$.
3) $\log_{10}(g_{rr})$ exhibits saturation behavior where initial g_{rr} equals 1 at the onset of charge release.

The complete mathematical formulation is presented in (28), with corresponding fitting parameters provided in Table VII and the fitting results graphically demonstrated in Fig. 15(b), showing excellent agreement across the entire operational range from initial charge formation to complete release

$$\log_{10} g_{rr} = \begin{cases} a\ln(b\log_{10}k_{\rm free}), \log_{10}k_{\rm free} \geq -0.2 \\ \min(c(\log_{10}k_{\rm free}+0.2)+d, 0), \log_{10}k_{\rm free} < -0.2 \end{cases}. \tag{28}$$

The reverse recovery charge Q_{rr} must be quantitatively correlated with key electrical parameters based on its underlying physical mechanisms. According to the physical analysis above, Q_{rr} shows strong dependence on both the current transition rate di_F/dt and forward current I_F, where I_F determines the initial minority carrier concentration during forward conduction. Higher I_F leads to greater carrier injection and consequently larger stored charge, resulting in significantly increased Q_{rr}. Simultaneously, faster di_F/dt during turn-OFF reduces leave more residual minority carriers and proportionally elevating Q_{rr}. These combined effects explain the observed experimental trends where Q_{rr} grows with both increasing I_F and di_F/dt.

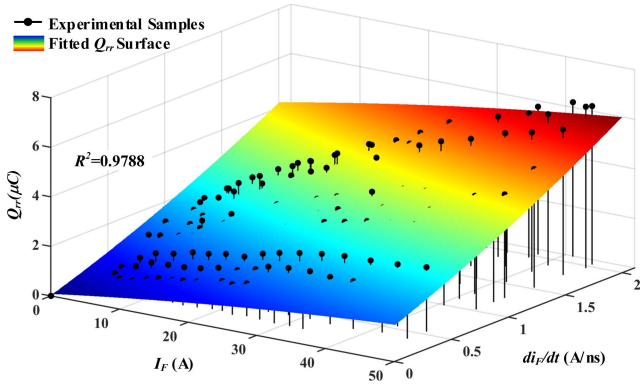

Fig. 16. Modeling of diode reverse recovery charge Q_{rr} versus I_F and current slew rate di_F/dt at $V_{\rm DC} = 650$ V.

At $V_{\rm DC} = 650$ V, the current transition slew rate di_F/dt and forward current I_F are modified through adjustment of gate drive resistance and pulse width parameters in DPT, enabling systematic extraction of Q_{rr} across various operating conditions. The comprehensive experimental results are presented as the characteristic scatter plot in Fig. 16.

The relationship between Q_{rr}, di_F/dt, and I_F can be accurately modeled using polynomial (29), based on MATLAB's Curve Fitting Toolbox [44]. The resulting coefficients are summarized in Table VII, and the three-dimensional fitted surface is visually presented in Fig. 16. An excellent coefficient of determination $R^2 = 0.978$ indicates high model accuracy as the value approaches 1.

The effect of $V_{\rm DC}$ should also be added to the Q_{rr} model. Fig. 17(a)–(f) compares the experimental and predicted results of Q_{rr} based on the model of (29) for a variation of $V_{\rm DC}$ in the range 300–800 V. Fig. 17 also display the root mean squared error (RMSE) between predicted and experimental results to show the prediction accuracy. When $V_{\rm DC}$ is higher than 650 V, the RMSE is small and the model has a very high prediction accuracy. However, as $V_{\rm DC}$ decreases, the RMSE becomes large, the model accuracy gradually deteriorates, and the model needs to be corrected. To further enhance model precision, only RMSE compensation is required

$$Q_{rr}\left(I_F, \frac{di}{dt}\right)\Big|_{V_{\rm DC}=650\ \rm V} = p_{00} + p_{10}I_F + p_{01}\frac{di}{dt} + p_{11}I_F\frac{di}{dt} + p_{20}I_F^2 + p_{02}\left(\frac{di}{dt}\right)^2. \tag{29}$$

Extracting the RMSE corresponding to different $V_{\rm DC}$ in Fig. 17(a)–(f), the relationship of RMSE with offset voltage ΔV (650 V as reference) can be obtained as shown in Fig. 17(g). The model can be well fitted with a linear function as in (30) with the parameters shown in Table VII. Up to this point, a complete

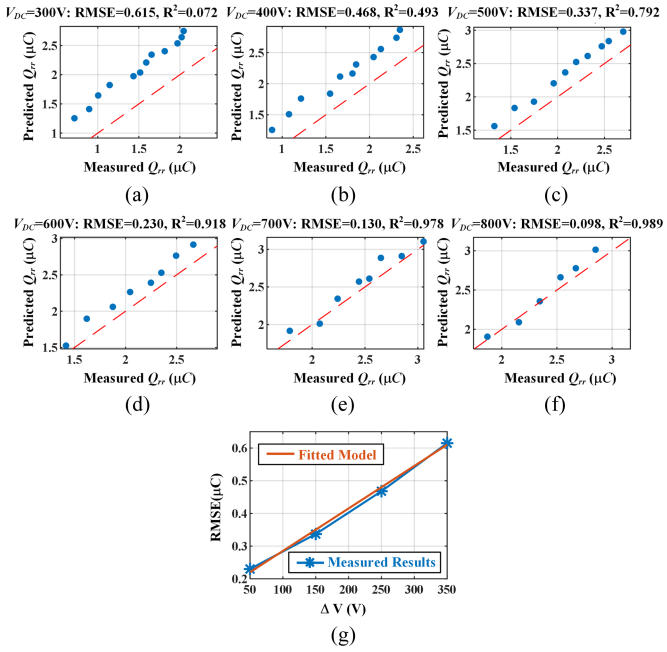

Fig. 17. Comparison of prediction and experimental results for Q_{rr} model under varying V_{DC} conditions. (a) $V_{\mathrm{DC}} = 300$ V. (b) $V_{\mathrm{DC}} = 400$ V. (c) $V_{\mathrm{DC}} = 500$ V. (d) $V_{\mathrm{DC}} = 600$ V. (e) $V_{\mathrm{DC}} = 700$ V. (f) $V_{\mathrm{DC}} = 800$ V. (g) Fitted model of RMSE versus ΔV.

expression for the reverse recovery charge subjected to V_{DC}, I_F and di_F/dt is obtained as (31).

The combination of (31) and (28) provides a universal method for incorporating reverse recovery characteristics into the model. However, integrating these dynamic characteristics into IGBT simulation models presents implementation challenges

$$\mathrm{RMSE}\left(V_{\mathrm{DC}}\right) = \begin{cases} 0, V_{\mathrm{DC}} \geq 650 \\ p_1\left(V_{\mathrm{DC}} - 650\right) + p_0, V_{\mathrm{DC}} < 650 \end{cases} \tag{30}$$

$$Q_{rr}\left(I_F, \frac{di}{dt}, V_{\mathrm{DC}}\right) = Q_{rr}\left(I_F, \frac{di}{dt}\right)\Big|_{V_{\mathrm{DC}}=650\ \mathrm{V}} - \mathrm{RMSE}\left(V_{\mathrm{DC}}\right). \tag{31}$$

The implementation of the dynamic reverse recovery conductance g_{rr} model is shown in Algorithm 2. Important inputs such as reverse voltage V_{DC}, forward current I_F, and current slew rate di_F/dt should be determined based on the previous pulse before the algorithm is calculated. Three functions are achieved in Algorithm 2.

1) When the diode forward voltage $-v_{\mathrm{CE}}$ transitions from positive to negative, the reverse recovery initiation moment is identified, the reverse recovery charge Q_{rr} is refreshed based on (31), and the released charge Q_{free} is initialized as 0. When the reverse recovery initiation is not detected, the previous reverse recovery charge Q_{rrB} is used and Q_{free} is updated through numerical integration $Q_{\mathrm{free}} = Q_{\mathrm{free}\,B} + dt{*}i_{rrB}$ with previously released charge Q_{rrB}.
2) The released charge percentage k_{free} is derived based on (27). Subsequently, the instantaneous reverse recovery conductance g_{rr} is determined using (28).

Algorithm 2: Dynamic Reverse Recovery Conductance Refresh and Calculation Logic.

Input:
$\boldsymbol{v_{CE}}$, $\boldsymbol{v_{CEB}}$ // Collector-emitter voltage (current, previous)
$\boldsymbol{Q_{freeB}}$ // Previously released charge
$\boldsymbol{Q_{rrB}}$ //Previous reverse recovery charge
$\boldsymbol{i_{rrB}}$ //Previous reverse recovery current
$\boldsymbol{v_{DC}}$ // Detected turn-off voltage
$\boldsymbol{di_F/dt}$ // Detected diode current slew rate
$\boldsymbol{I_F}$ // Detected forward current
$\boldsymbol{dt}$ //Current simulation timestep

Output:
$\boldsymbol{g_{rr}}$ //Reverse recovery conductance
$\boldsymbol{i_{rr}}$ //Reverse recovery current
$\boldsymbol{Q_{free}}$ //Current released charge
$\boldsymbol{Q_{rr}}$ //Total recovery charge

1.If $\boldsymbol{v_{CE}} > 0$ AND $\boldsymbol{v_{CEB}} < 0$:
– Refresh reverse recovery parameters
– Calculate $\boldsymbol{Q_{rr}}$ using (31): $\boldsymbol{Q_{rr}}$ ($\boldsymbol{I_F}$, $\boldsymbol{di_F/dt}$, $\boldsymbol{V_{DC}}$)
– Set $\boldsymbol{Q_{free}} = 0$
Else: Use previous reverse recovery parameters
– $\boldsymbol{Q_{rr}} = \boldsymbol{Q_{rrB}}$.
–Calculate $\boldsymbol{Q_{free}}$ using (25): $\boldsymbol{Q_{free}} = \boldsymbol{Q_{freeB}} + \boldsymbol{dt} * \boldsymbol{i_{rrB}}$.
End

2. If $\boldsymbol{Q_{rr}} \neq 0$:
– Calculate released charge percentage $\boldsymbol{k_{free}} = \boldsymbol{Q_{free}}/\boldsymbol{Q_{rr}}$
– Calculate conductance $\boldsymbol{g_{rr}}$ using (28)
Else:
– $\boldsymbol{g_{rr}} = 0$
– $\boldsymbol{k_{free}} = 1$. End

3. Output current:
$\boldsymbol{i_{rr}} = \boldsymbol{g_{rr}} * \boldsymbol{v_{CE}}$

3) The reverse recovery current $i_{rr} = g_{rr}{*}v_{\mathrm{CE}}$ is output. The simplified pseudocode representation is shown in Algorithm 2.

Since the components and functions required by the proposed model are very simple and have already been installed in common circuit simulation software library, the proposed model can be integrated with the popular power electronics simulation software.

V. Experimental Verification

A. Experimental Platform

The experimental platform is shown in Fig. 18, and the A-phase bridge arm of the FS50R12KT4 IGBT module from Infineon Technologies is used for the double-pulse test, and the test equipment is shown in Table VIII. The bus loop is as small as possible, and the bus parasitic inductor can be modified with external coil as shown in pink.

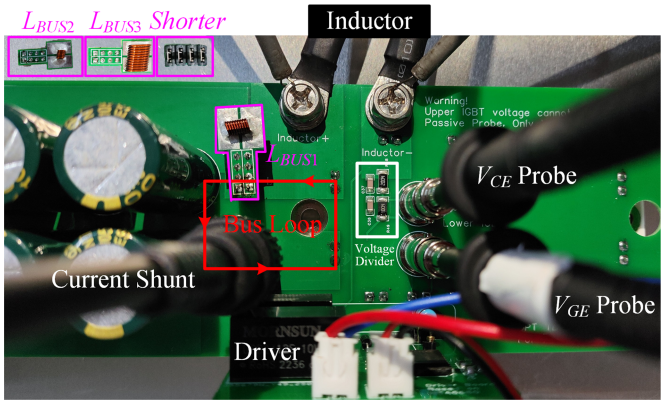

Fig. 18. Double-pulse test platform.

TABLE VIII
TYPES AND PARAMETERS OF EXPERIMENT INSTRUMENTS

Instruments	Types	Parameters
HV DC source	EA-PSI81500-30 3U	1500 V /30 A
LISN CISPR32	NNLK 8122 (150kHz-30MHz)	1000 V/50 A
Oscilloscope	SDS3054X	500 MHz
Voltage Probes	CYBERTEK/DP6150B	200 MHz, 1500 V
	SIGLENT/SP3050A+Voltage divider network	500 MHz, 1200 V
Current Probes	CYBERTEK/CSD005M10	1 GHz
IGBT Module	Infineon/FS50R12KT4_B15	1200 V/50 A
	Mitsubishi Electric/CM100DY-24T	1200 V/100 A
Driver Board	Driver chip: HSA6880	
	Isolated Source: QA03	+15 V ~ −8 V
Inductor	Ferrosilicon Aluminum Core	L = 1 mH
CM chokes	NiZn core: DN85H, DMEGC	μ = 850
	MnZn core: R7K, DMEGC	μ = 7000

To validate the high accuracy and general applicability of the proposed dynamic IGBT model incorporating turn-OFF bulk resistance and turn-ON reverse recovery conductance, ten operating conditions with different dc voltages, load currents, driver resistances, bus parasitic inductors, and switching device are selected for experimental and simulation verification, as shown in Table IX. The another IGBT selected is CM100DY-24T from Mitsubishi Electric with different technology. CM100DY-24T released at 2020.10 uses IGBT7 T7 technology [45], which is much advanced to T4 technology used by FS50R12KT4_B15 at 2013.11 [34]. The proposed model is also applied to the newer devices for applicability verification. The parasitic inductors are selected from 35 to 400 nH, and the driver resistances are selected from 91 to 5 Ω, which covers most application scenarios.

Comparative results of the existing model, the proposed model, and experimental measurements, including waveform and quasi-peak spectrum comparisons, are presented in Fig. 19. The spectrum processing parameters are listed in Table IV. All prediction errors are listed in Table IX.

B. Accuracy Verification of EMI Source Ringing

1) Turn-Off Ringing Accuracy Verification: For O1, the time-domain waveforms in Fig. 19 O1: (a) and (c) reveal that the proposed model demonstrates superior agreement with experimental measurements compared to the existing model. The turn-OFF voltage ringing attenuation shows remarkable consistency with experimental data, due to the time-varying bulk resistance characterization. Spectral analysis in Fig. 19 O1: (e) further quantifies these improvements: The lower IGBT voltage ringing spectrum achieves exceptional 0.006 dB deviation from experimental results, representing a 5 dB accuracy enhancement over existing model (5 dB error).

For O2 with lower I_L, $V_{\mathrm{CE\_}PK}$ is reduced resulting in stronger damping effect, based on (18). Fig. 19 O2 (a) and (c) demonstrate the proposed model's exceptional capability in predicting ringing. The proposed model successfully captures the smaller ringing characteristics where reduced I_L leads to both lower peak ringing voltage and thus faster damping transients enabled by its dynamic bulk resistance. The existing model fails to reproduce the damping effect. Spectral performance in Fig. 19 O2 (e) still establishes good accuracy: The $v_{\mathrm{CE}L}$ spectrum of the proposed model shows merely 6 dB deviation from measurements, representing an 14 dB error reduction versus existing model (20 dB error).

For O3 with lower V_{DC}, $v_{\mathrm{CE\_}PK}$ is reduced resulting in stronger damping effect. Fig. 19 O3 (a) and (c) demonstrates critical turn-OFF ringing improvements in the time-domain waveforms compared to the existing model. The proposed model achieves precise matching of the experimentally observed fast ringing attenuation in turn-OFF ringing, while the existing model does not. Spectral analysis in Fig. 19 O3 (e) reveals good performance enhancements: the $v_{\mathrm{CE}L}$ spectrum of the proposed model shows merely 6dB deviation from measurements, representing an 18dB error reduction versus existing model (24 dB error).

For O4 with bigger gate resistance, di_C/dt is reduced, thus $v_{\mathrm{CE\_}PK}$ is reduced, resulting in stronger damping effect. Fig. 19 O4 (a) and (c) demonstrates the proposed model's good capability in predicting turn-OFF ringing waveforms. Spectral performance in Fig. 19 O4 (e) shows good accuracy: the lower IGBT voltage spectrum of the proposed model shows merely 4 dB deviation from measurements. The error may come from the smaller $v_{\mathrm{CE\_}PK}$ than the experimental results.

For O5–O8: (a), (c), (e) with smaller parasitic inductances in Fig. 19, the turn-OFF ringing has a smaller amplitude and higher frequency. For O5–O6: (a), (c), (e), due to the small ringing peak, the R_{CE} is large and the ringing damping is strong. Therefore, the proposed model with dynamic R_{CE} reduces the prediction error by up to 17 dB compared to existing models. For O7–O8: (a), (c), (e), the ringing frequencies have reached the RE band, and the oscillation periods are very small or even nonexistent. The waveform predicted by proposed model and measured waveform no longer has turn-OFF ringing, while the prediction results of existing model still have. The $i_{\mathrm{CE}L}$ waveform errors of the proposed model in O7 (c) and O8 (c) are caused by the i_{tail} which increases significantly when the v_{GE} voltage changes rapidly by small R_G. The i_{tail} error has little effect on the $v_{\mathrm{CE}L}$ of the proposed model. Spectrum results show that the prediction

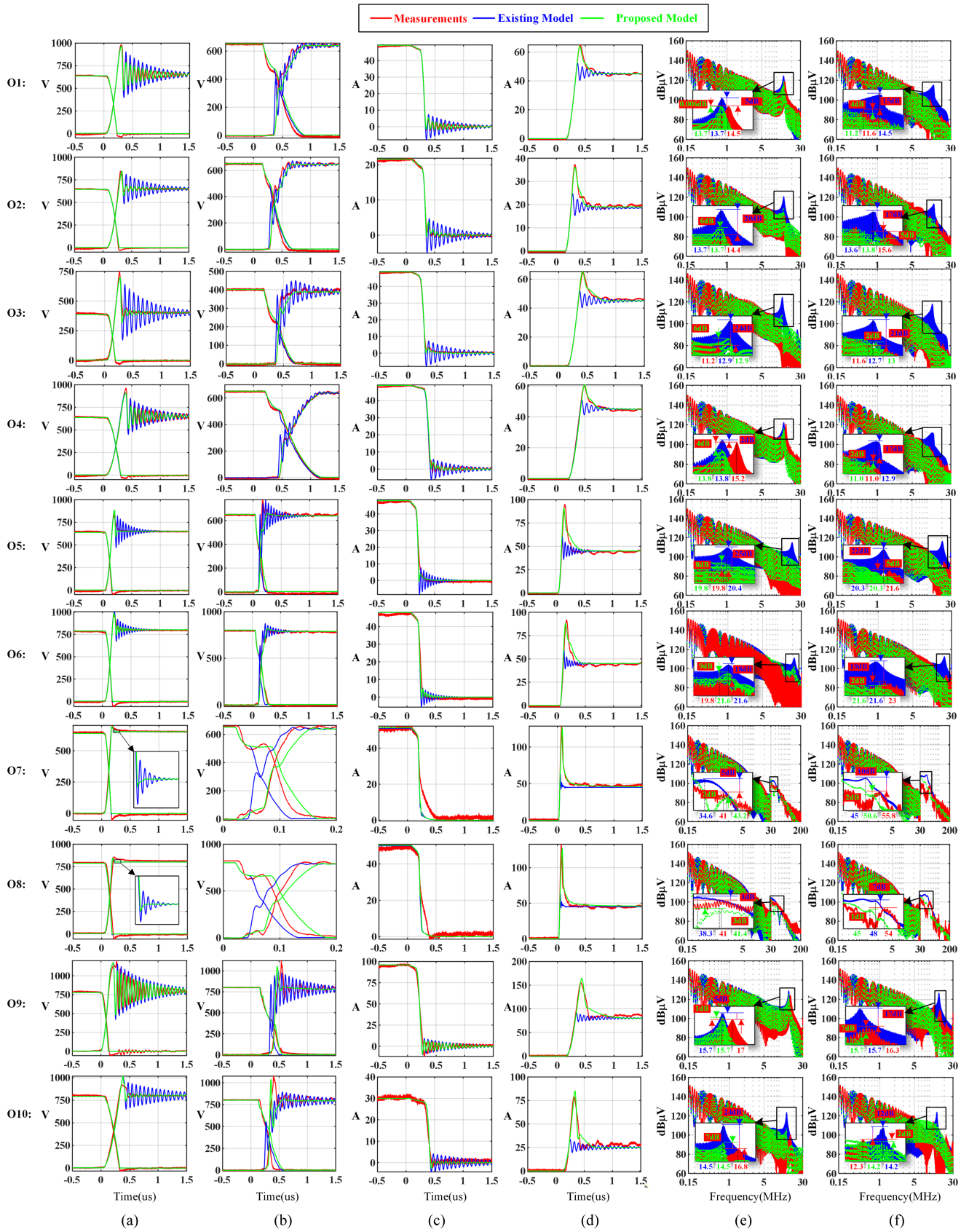

Fig. 19. Waveforms and QP spectra comparisons of the existing and proposed IGBT model at O1 – O10. (a) $v_{\mathrm{CE}\,L}$ and $v_{\mathrm{CE}\,U}$ during lower IGBT turn-OFF. (b) $v_{\mathrm{CE}\,L}$ and $v_{\mathrm{CE}\,U}$ during lower IGBT turn-ON. (c) $i_{\mathrm{CE}\,L}$ during lower IGBT turn-OFF. (d) $i_{\mathrm{CE}\,L}$ during lower IGBT turn-ON. (e) $v_{\mathrm{CE}\,L}$ spectrum characterizing turn-OFF ringing. (f) $\mathrm{v_{CEU}}$ spectrum characterizing turn-ON ringing.

TABLE IX
RING ERROR COMPARISON BETWEEN EXISTING AND PROPOSED MODELS AGAINST EXPERIMENTAL RESULTS

Operating Condition	Switching Device	V_{DC}	I_{ON}	I_{OFF}	R_G	L_{BUS}	Existing Model (turn-off, turn-on, system)	Proposed Model (turn-off, turn-on, system)	Accuracy Improvement (turn-off, turn-on, system)
O1	FS50R12KT4_B15	650 V	45 A	50 A	56 ohms	400 nH	(5 dB, 15 dB, 8 dB)	(0.006 dB, 4 dB, 1 dB)	(5 dB, 11 dB, 7 dB)
O2		650 V	20 A	20 A	56 ohms	400 nH	(20 dB, 17 dB, 17dB)	(6 dB, 5 dB, 5dB)	(14 dB, 12 dB, 12 dB)
O3		400 V	45 A	50 A	56 ohms	400 nH	(24 dB, 21 dB, 22dB)	(6 dB, 2 dB, 5dB)	(18 dB, 19 dB, 17 dB)
O4		650 V	45 A	50 A	91 ohms	400 nH	(2 dB, 17 dB, 4 dB)	(4 dB, 2 dB, 3 dB)	(-2 dB, 15 dB, 1 dB)
O5		650 V	45 A	50 A	15 ohms	180 nH	(25 dB, 22 dB, 23dB)	(8 dB, 5 dB, 6 dB)	(17 dB, 17 dB, 17 dB)
O6		800 V	45 A	50 A	15 ohms	180 nH	(18 dB, 19 dB, 18 dB)	(9 dB, 2 dB, 5 dB)	(9 dB, 17 dB, 13 dB)
O7		650 V	45 A	50 A	5 ohms	35 nH	(5 dB, 10 dB, -)	(2 dB, 2 dB, -)	(3 dB, 7 dB, -)
O8		800 V	45 A	50 A	5 ohms	35 nH	(1 dB, 7 dB, -)	(3 dB, 1 dB, -)	(-2 dB, 6 dB, -)
O9	CM100DY-24T	800V	80A	96A	15 ohms	400 nH	(5 dB, 17 dB, 8 dB)	(1 dB, 7 dB, 2 dB)	(4 dB, 10 dB, 6 dB)
O10		800V	25A	30A	15 ohms	400 nH	(24 dB, 12 dB, 14 dB)	(7 dB, 2 dB, 2 dB)	(17 dB, 10 dB, 12 dB)

error of the proposed model is 3 dB smaller than that of existing models.

For O9–O10: (a), (c), (e) with different IGBT CM100DY-24T in Fig. 19, the turn-OFF ringing still exhibits time-varying damping phenomenon. The turn-OFF ringing prediction accuracy of the existing model is only 5 dB under heavy load (O9), but the error reaches 24 dB under light load (O10). This is because under heavy load, v_{CE_PK} is large, R_{CE} is small, and damping is small, while under light load, v_{CE_PK} is small, R_{CE} is large, and damping is large. However, the proposed model, which takes into account dynamic bulk resistance, has a turn-OFF ringing error of less than 7 dB at O9–O10.

2) Turn-On Ringing Accuracy Verification: For O1, the time-domain waveforms in Fig. 19 O1: (b) and (d) reveal that the proposed model demonstrates better agreement with experimental measurements compared to the existing model. The turn-ON current waveform of lower IGBT exhibits better matching with measured results. The wrong turn-ON ringing in upper IGBT voltage is effectively eliminated. Spectral analysis in Fig. 19 O1: (f) further quantifies these improvements: the upper IGBT voltage spectrum shows only 4 dB discrepancy versus measurements, corresponding to an 11 dB improvement compared to existing model (15 dB error).

For O2 with lower I_L, Q_{rr} is reduced based on (29). Fig. 19 O2: (b) and (d) demonstrate the proposed model's exceptional capability in predicting turn-ON ringing. The proposed model maintains accurate prediction of reverse recovery current and charge reduction under decreasing I_L conditions. The proposed model achieves higher accuracy than existing model in simulating the V_{CE} of the upper IGBT during the turn-ON period of the lower IGBT. Spectral performance in Fig. 19 O2: (f) still establishes good accuracy: The upper IGBT spectrum accuracy reaches 5 dB with 12 dB improvement over existing model (17 dB error). These results verify the model's good ability to maintain precision across varying load conditions.

For O3 with lower V_{DC}, Q_{rr} is reduced based on (31). Fig. 19 O3: (b) and (d) demonstrate the improvements in the time-domain waveforms compared to the existing model. Both the lower IGBT current and the upper IGBT voltage waveform when lower IGBT turns ON show significantly improved accuracy compared with the existing model. Spectral analysis in Fig. 19 O3: (f) reveals good performance enhancements: The upper IGBT voltage spectrum achieves exceptional 2 dB accuracy, corresponding to a 19 dB improvement over the existing model (21 dB error).

For O4 with larger gate resistance, di_F/dt is reduced, thus Q_{rr} is reduced based on (29). Fig. 19 O4: (b) and (d) demonstrate the proposed model's good capability in predicting turn-ON ringing, when R_g is increased. The proposed model maintains accurate prediction of reverse recovery current and charge reduction under decreasing di_F/dt conditions. The upper IGBT voltage of the proposed model matches the experimental measurements very well, while the existing model does not. Spectral performance in Fig. 19 O4: (f) shows good accuracy: the upper IGBT voltage spectrum shows merely a 2 dB deviation from measurements, representing a 15 dB error reduction versus the existing model (17 dB error).

For O5–O8: (b), (d), (f) with smaller parasitic inductances in Fig. 19, the reverse recovery currents become much larger, and the turn-ON ringing is still relatively small. The proposed model with dynamic g_{rr} predicts the reverse recovery current and damping effect of g_{rr} well, while existing model cannot. For O7–O8: (b), (d), the ringing frequencies have reached the RE band, and the oscillation periods are very small or even nonexistent. The waveform predicted by proposed model and measured waveform no longer has turn-ON ringing, while the prediction results of existing model still have. Spectrum results show that the prediction error of the proposed model is 7 dB smaller than that of existing models.

For O9–O10: (b), (d), (f) with different IGBT CM100DY-24T in Fig. 19, reverse recovery conductance g_{rr} also has a significant effect on the damping of turn-ON ringing. The proposed model takes into account dynamic g_{rr}, with a turn-ON ringing error within 7 dB. However, the turn-OFF ringing predicted by the existing model significantly exceeds the measured value, with an error of up to 17 dB.

C. Accuracy Verification of System EMI Ringing

To demonstrate the practical benefit on EMI prediction of the proposed model, system-level conducted EMI tests with EMI filter are performed, as shown in Fig. 20. The IGBT module is at the bottom of the printed circuit board, and the IGBT heatsink is connected to the aluminum ground, which is also called protect earth. Two CM chokes are used as the EMI filter. The system EMI are measured at LISN's 50-Ω port.

The impedances of the parasitic capacitance and CM choke are extracted by the impedance analyzer 4294 A. Then, time-domain simulation circuits containing the proposed model and existing model are constructed separately in MATLAB / Simulink, with which system EMI can be predicted.

The prediction results of operating condition O1 and O2 are shown in Fig. 21, both of which contains the LISN voltage

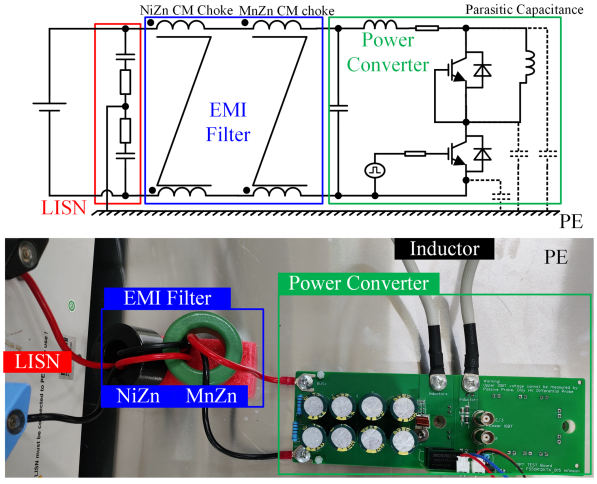

Fig. 20. System level EMI test platform: diagram and photograph.

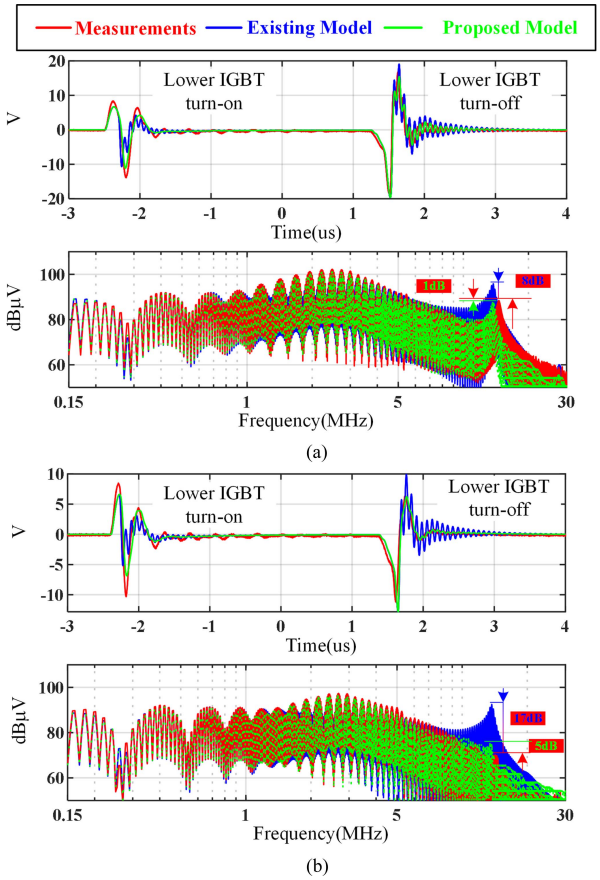

Fig. 21. System EMI waveform and spectra comparison of existing and proposed IGBT model at operating condition O1 and O2, (a) O1, (b) O2.

waveforms of one switching cycle and EMI spectra based on EN55032 in Table IV.

At O1, When the lower IGBT turns ON, the predicted LISN waveform of the proposed model matches the experimental results very well, while the existing model exhibits incorrect oscillations. When the lower IGBT is turned OFF, the predicted results of both models match the experimental results, but the proposed model is closer to the experimental results. The spectrum results of the system EMI also show that the prediction

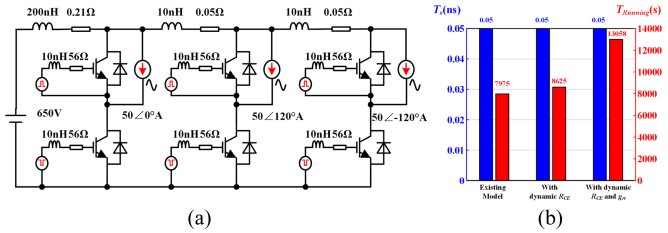

Fig. 22. Validation of simulation stability and solver performance. (a) 3ph-2L inverter circuit model in MATLAB / Simulink. (b) Required time step T_s and running time T_{running}.

error of the proposed model is 1 dB, which is 7 dB smaller than the 8 dB prediction error of the existing model.

At O2, When the lower IGBT turns ON, the predicted LISN waveform of the proposed model matches the experimental results very well, while the existing model exhibits incorrect oscillations. When the lower IGBT turns OFF, the proposed model and experimental results are in good agreement, while the existing model exhibits excessive oscillations. The spectrum results of the system EMI also demonstrate that the prediction error of the proposed model is 5 dB, which is 12 dB smaller than the 17 dB prediction error of the existing model.

It can also be seen that the system EMI is essentially the linear average of the turn-ON and turn-OFF EMI. Since the turn-OFF waveform has a larger amplitude and a steeper slope than the turn-ON waveform, the turn-OFF waveform spectrum dominates the system EMI. Therefore, the predicted system EMI error is usually close to the error of the turn-OFF EMI source. More system EMI results are summarized in Table IX, which also verify this analysis. The system EMI results of O7 and O8 are empty, because the ringing frequency has been in radiated EMI band and cannot be tested by conducted EMI platform.

D. Verification of Simulation Stability and Solver Performance

In order to further verify the impact of the time-varying dynamic parameters on the simulation stability and solver performance, the proposed IGBT model with and without dynamic parameters is applied to a three-phase two-level (3ph-2L) inverter circuit with 20 ms simulation time for simulation verification, as shown in Fig. 22(a). The changes in the step size T_s required for the simulation and the simulation running time T_{running} with the addition of different parameters are compared in Fig. 22(b).

The simulation stability can be characterized by the step size T_s required for simulation [46], because the more unstable the simulation model, the smaller the step size required. As shown in the blue box of Fig. 22(b), the required step size T_s is not affected by the dynamic parameters added. Therefore, the added dynamic parameters have no effect on the simulation stability.

The solver performance can be characterized as simulation running time T_{running}. The simulation running time before and after the introduction of dynamic parameters are shown in the red box of Fig. 22(b). The results show that the dynamic bulk resistance parameter R_{CE} has little effect on the solver performance, while the introduction of the dynamic reverse recovery conductance parameter g_{rr} affects the solver performance to a greater extent. This is due to the fact that the g_{rr} parameter has

more variables associated with it and is more complex to logic and compute.

VI. Conclusion

Existing switching device behavioral models have poor accuracy in characterizing Si IGBT ringing effects, which are important to EMI prediction. Dynamic bulk resistance and reverse recovery conductance are identified as the dominant factors affecting turn-OFF and turn-ON ringing accuracy, respectively. The peak voltage is identified as the dominant factor affecting the bulk resistance, and the reverse recovery conductance is affected by both $V_{\rm DC}$, I_F, di_F/dt. The proposed dynamic IGBT model is developed by extending the existing model with dynamic bulk resistance and reverse recovery conductance. CE test experiments under ten distinct operating conditions demonstrate that the proposed model achieves up to 19 and 17 dB improvements in EMI source and system EMI ringing accuracy, respectively, compared to the existing model.

The proposed dynamic Si IGBT model has the advantages of high accuracy, user-friendliness, good stability, and universal adaptability to diverse operating conditions and various IGBT device types. The model can be integrated with popular power electronics simulation software like Simulink, SABER, Pspice, and is expected to be widely used in the EMI prediction of various power electronic systems.

Appendix

A. Measurement Method of the Interterminal Capacitances

The capacitances of switching devices essentially form a two-port network, as illustrated in Fig. 23. This two-port network can be fully characterized by its *S*-parameters. Based on the conversion relationship between the Π-network and *S*-parameters, the expressions for each capacitance can be derived, as shown in (A1), (A2), and (A3). All *S*-parameters are complex-valued. To measure these capacitances, the center conductor of Port 1 of the network analyzer is connected to the collector (C), while the reference grounds of Port 1 and Port 2 are all connected to the emitter (E). The center conductor of Port 2 is connected to the gate (G). By enabling the voltage bias sweep on Port 1, the *S*-parameters can be obtained as a function of $v_{\rm CE}$, allowing the extraction of the interterminal capacitance curves in a single voltage bias sweep based on (A1), (A2), and (A3). The results of the measured *S* parameters are shown in Fig. 24 and the configuration of the network analyzer are detailed in Fig. 23. Capacitance of MOSFET can also be obtained based on the extraction method

$$C_{\rm CE}=1/{\rm Im}\left(-\frac{50\left(-S_{21}^2+S_{11}+S_{22}+S_{11}S_{22}+1\right)}{-S_{21}^2+2S_{21}+S_{11}-S_{22}+S_{11}S_{22}-1}\right)/j2\pi f \tag{A1}$$

$$C_{\rm GE}=1/{\rm Im}\left(\frac{50\left(-S_{21}^2+S_{11}+S_{22}+S_{11}S_{22}+1\right)}{S_{21}^2-2S_{21}+S_{11}-S_{22}-S_{11}S_{22}+1}\right)/j2\pi f \tag{A2}$$

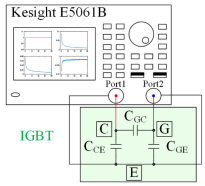

Parameters	Values
Center frequency	100kHz
DC bias port	Port1
Voltage Sweep	[0,40] V
Power	0dBm
Calibration	Full 2-Port

Fig. 23. Interterminal capacitance extraction method based on *S*-parameters.

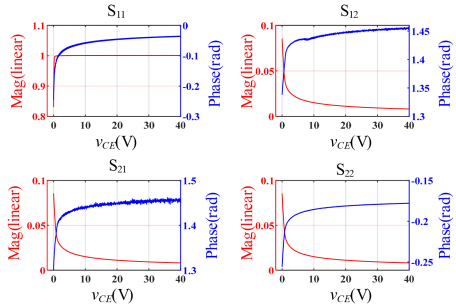

Fig. 24. S-parameters under different $v_{\rm CE}$.

$$C_{\rm GC}=1/{\rm Im}\left(\frac{25\left(-S_{21}^2+S_{11}+S_{22}+S_{11}S_{22}+1\right)}{S_{21}}\right)/j2\pi f. \tag{A3}$$

References

[1] Y. Yu, P. Zhou, X. Pei, D. Zhao, Q. Chen, and Y. Zhang, "Modeling and analysis of multi-source spectrum in PV inverter considering EMI accumulation effect," in *Proc. IEEE 2nd Int. Power Electron. Appl. Symp.*, 2023, pp. 1750–1756, doi: 10.1109/PEAS58692.2023.10394861.

[2] European Committee for Electrotechnical Standardization, "EN 55011:2016/A1:2017+A11:2020 industrial, scientific and medical equipment - radio-frequency disturbance characteristics - limits and methods of measurement," CENELEC, Brussels, Belgium, 2020.

[3] International Electrotechnical Commission, "CISPR 11:2023 Industrial, scientific and medical equipment - radio-frequency disturbance characteristics - limits and methods of measurement," IEC, Geneva, Switzerland, 2023.

[4] Y. Yu, X. Pei, P. Zhou, Q. Chen, and D. Zhao, "Analysis and decoupling of multisource EMI in high-power PV inverter," *IEEE Trans. Power Electron.*, vol. 39, no. 10, pp. 13096–13106, Oct. 2024, doi: 10.1109/TPEL.2024.3416693.

[5] Z. Ma, S. Wang, H. Sheng, and S. Lakshmikanthan, "Modeling, analysis and mitigation of radiated EMI due to PCB ground impedance in a 65 W high-density active-clamp flyback converter," *IEEE Trans. Ind. Electron.*, vol. 70, no. 12, pp. 12267–12277, Dec. 2023, doi: 10.1109/TIE.2023.3239904.

[6] Q. Yang et al., "Analysis and optimization of high-frequency switching oscillation conducted CM current considering parasitic parameters based on a half-bridge power module," *IEEE Trans. Power Electron.*, vol. 38, no. 10, pp. 12659–12674, Oct. 2023, doi: 10.1109/TPEL.2023.3291893.

[7] J. Yao, S. Wang, and Z. Luo, "Modeling, analysis, and reduction of radiated EMI due to the voltage across input and output cables in an automotive non-isolated power converter," *IEEE Trans. Power Electron.*, vol. 37, no. 5, pp. 5455–5465, May 2022, doi: 10.1109/TPEL.2021.3128628.

[8] L. Yang, H. Zhao, S. Wang, and Y. Zhi, "Common-mode EMI noise analysis and reduction for AC–DC–AC systems with paralleled power modules," *IEEE Trans. Power Electron.*, vol. 35, no. 7, pp. 6989–7000, Jul. 2020, doi: 10.1109/TPEL.2019.2957358.

[9] Y. Li, H. Zhang, S. Wang, H. Sheng, C. P. Chng, and S. Lakshmikanthan, "Investigating switching transformers for common mode EMI reduction to remove common mode EMI filters and Y-capacitors in flyback converters," *IEEE J. Emerg. Sel. Topics Power Electron.*, vol. 6, no. 4, pp. 2287–2301, Dec. 2018, doi: 10.1109/JESTPE.2018.2827041.

[10] D. Han, S. Li, Y. Wu, W. Choi, and B. Sarlioglu, "Comparative analysis on conducted CM EMI emission of motor drives: WBG versus Si devices," *IEEE Trans. Ind. Electron.*, vol. 64, no. 10, pp. 8353–8363, Oct. 2017, doi: 10.1109/TIE.2017.2681968.
[11] P. Tian, F. Chen, T. M. Jahns, and B. Sarlioglu, "The effect of gate drive resistance on the CM EMI performance of the balanced inverter with asymmetrical parasitic impedance distribution," *IEEE Trans. Ind. Appl.*, vol. 60, no. 6, pp. 9052–9065, Nov./Dec. 2024, doi: 10.1109/TIA.2024.3446748.
[12] R. Zhang, W. Chen, Y. Zhou, Z. Shi, R. Yan, and X. Yang, "Mathematical modeling of EMI spectrum envelope based on switching transient behavior," *IEEE J. Emerg. Sel. Topics Power Electron.*, vol. 10, no. 2, pp. 2497–2515, Apr. 2022, doi: 10.1109/JESTPE.2021.3109040.
[13] J. Wang, H. S. H. Chung, and R. T. H. Li, "Characterization and experimental assessment of the effects of parasitic elements on the MOSFET switching performance," *IEEE Trans. Power Electron.*, vol. 28, no. 1, pp. 573–590, Jan. 2013, doi: 10.1109/TPEL.2012.2195332.
[14] B. Zhang, S. Wang, Y. Lai, and Y. Yang, "Modeling and prediction of low-frequency radiated EMI for a SiC motor drive system," *IEEE Trans. Ind. Electron.*, vol. 71, no. 9, pp. 10210–10220, Sep. 2024, doi: 10.1109/TIE.2023.3329226.
[15] Z. Ma, Y. Pei, L. Wang, Q. Yang, Z. Qi, and G. Zeng, "An accurate analytical model of SiC MOSFETs for switching speed and switching loss calculation in high-voltage pulsed power supplies," *IEEE Trans. Power Electron.*, vol. 38, no. 3, pp. 3281–3297, Mar. 2023, doi: 10.1109/TPEL.2022.3219241.
[16] B. Hao, Y. Yang, X. Tang, and Z. Zhao, "Transient analytical model of high-voltage and high-power IGBT device based on nondual relationship for the switching process," *IEEE Trans. Power Electron.*, vol. 38, no. 3, pp. 2827–2832, Mar. 2023, doi: 10.1109/TPEL.2022.3219258.
[17] Q. Yang, L. Wang, Z. Ma, X. Lu, H. Wang, and Z. Qi, "Calculation and analysis of the dynamic turn-on process of SiC MOSFET based on a piecewise linearization method," *IEEE J. Emerg. Sel. Topics Power Electron.*, vol. 12, no. 4, pp. 3948–3966, Aug. 2024, doi: 10.1109/JESTPE.2024.3410396.
[18] S. K. Roy and K. Basu, "Analytical model to study hard turn-off switching dynamics of SiC MOSFET and Schottky Diode pair," *IEEE Trans. Power Electron.*, vol. 36, no. 1, pp. 861–875, Jan. 2021, doi: 10.1109/TPEL.2020.2998873.
[19] Y. Xie, C. Chen, Y. Yan, Z. Huang, and Y. Kang, "Investigation on ultralow turn-off losses phenomenon for SiC MOSFETs with improved switching model," *IEEE Trans. Power Electron.*, vol. 36, no. 8, pp. 9382–9397, Aug. 2021, doi: 10.1109/TPEL.2021.3050544.
[20] M. Jin and M. Weiming, "Power converter EMI analysis including IGBT nonlinear switching transient model," *IEEE Trans. Ind. Electron.*, vol. 53, no. 5, pp. 1577–1583, Oct. 2006, doi: 10.1109/TIE.2006.882009.
[21] B. Shi, Z. Zhao, and Y. Zhu, "Piecewise analytical transient model for power switching device commutation unit," *IEEE Trans. Power Electron.*, vol. 34, no. 6, pp. 5720–5736, Jun. 2019, doi: 10.1109/TPEL.2018.2867735.
[22] Z. Dong, X. Wu, H. Xu, N. Ren, and K. Sheng, "Accurate analytical switching-on loss model of SiC MOSFET considering dynamic transfer characteristic and Qgd," *IEEE Trans. Power Electron.*, vol. 35, no. 11, pp. 12264–12273, Nov. 2020, doi: 10.1109/TPEL.2020.2988899.
[23] X. Wang, Z. Zhao, K. Li, Y. Zhu, and K. Chen, "Analytical methodology for loss calculation of SiC MOSFETs," *IEEE J. Emerg. Sel. Topics Power Electron.*, vol. 7, no. 1, pp. 71–83, Mar. 2019, doi: 10.1109/JESTPE.2018.2863731.
[24] A. R. Hefner and D. M. Diebolt, "An experimentally verified IGBT model implemented in the Saber circuit simulator," *IEEE Trans. Power Electron.*, vol. 9, no. 5, pp. 532–542, Sep. 1994, doi: 10.1109/63.321038.
[25] M. Turzynski and W. J. Kulesza, "A simplified behavioral MOSFET model based on parameters extraction for circuit simulations," *IEEE Trans. Power Electron.*, vol. 31, no. 4, pp. 3096–3105, Apr. 2016, doi: 10.1109/TPEL.2015.2445375.
[26] H. Li, X. Zhao, K. Sun, Z. Zhao, G. Cao, and T. Q. Zheng, "A non-segmented PSPICE model of SiC MOSFET with temperature-dependent parameters," *IEEE Trans. Power Electron.*, vol. 34, no. 5, pp. 4603–4612, May 2019, doi: 10.1109/TPEL.2018.2865611.
[27] L. Han, L. Liang, Y. Wang, X. Tang, and Y. Du, "A SiC IGBT model with accurate static and dynamic tracking capability," *IEEE Trans. Electron Devices*, vol. 69, no. 7, pp. 3833–3840, Jul. 2022, doi: 10.1109/TED.2022.3175946.
[28] K. Chen, Z. Zhao, L. Yuan, T. Lu, and F. He, "The impact of nonlinear junction capacitance on switching transient and its modeling for SiC MOSFET," *IEEE Trans. Electron Devices*, vol. 62, no. 2, pp. 333–338, Feb. 2015, doi: 10.1109/TED.2014.2362657.
[29] Z. Duan, T. Fan, X. Wen, and D. Zhang, "Improved SiC power MOSFET model considering nonlinear junction capacitances," *IEEE Trans. Power Electron.*, vol. 33, no. 3, pp. 2509–2517, Mar. 2018, doi: 10.1109/TPEL.2017.2692274.
[30] N. Wang, J. Zhang, and F. Deng, "Improved SiC MOSFET model considering channel dynamics of transfer characteristics," *IEEE Trans. Power Electron.*, vol. 38, no. 1, pp. 460–471, Jan. 2023, doi: 10.1109/TPEL.2022.3200456.
[31] B. W. Nelson et al., "Computational efficiency analysis of SiC MOSFET models in SPICE: Dynamic behavior," *IEEE Open J. Power Electron.*, vol. 2, pp. 106–123, 2021, doi: 10.1109/OJPEL.2021.3056075.
[32] MathWorks, "Simscape electrical - IGBT model," MathWorks Documentation, R2023a, 2025. [Online]. Available: https://www.mathworks.com/help/releases/R2023a/sps/powersys/ref/IGBT.html?s_tid=doc_srchtitle
[33] Ansys Inc., "Characterization of Simplorer | Webinar," Ansys Resource Center, 2025. [Online]. Available: https://www.ansys.com/zh-cn/resource-center/webinar/characterization-of-simplorer
[34] "FS50R12KT4 1200 V IGBT module datasheet," Infineon Technologies AG, Neubiberg, Germany, Rev. 2.4, 2021. [Online]. Available: https://www.infineon.com/dgdl/Infineon-FS50R12KT4_B11-DS-v03_00-en_cn.pdf?fileId=db3a30433de4e67f013deed32b2b39f8
[35] R. Stark, A. Tsibizov, N. Nain, U. Grossner, and I. Kovacevic-Badstuebner, "Accuracy of three interterminal capacitance models for SiC power MOSFETs under fast switching," *IEEE Trans. Power Electron.*, vol. 36, no. 8, pp. 9398–9410, Aug. 2021, doi: 10.1109/TPEL.2021.3053330.
[36] S. Jimenez, A. Lemmon, B. Nelson, and B. Deboi, "Comprehensive characterization of MOSFET intrinsic capacitances," in *Proc. IEEE Appl. Power Electron. Conf. Expo.*, 2021, pp. 1524–1530, doi: 10.1109/APEC42165.2021.9487289.
[37] U. Kundu and P. Sensarma, "Accurate estimation of diode reverse-recovery characteristics from datasheet specifications," *IEEE Trans. Power Electron.*, vol. 33, no. 10, pp. 8220–8225, Oct. 2018, doi: 10.1109/TPEL.2018.2811380.
[38] D. Menzi, D. Bortis, and J. W. Kolar, "EMI filter design for a three-phase buck–boost Y-inverter VSD with unshielded motor cables considering IEC 61800-3 conducted and radiated emission limits," *IEEE Trans. Power Electron.*, vol. 36, no. 11, pp. 12919–12937, Nov. 2021, doi: 10.1109/TPEL.2021.3075785.
[39] Y. Yu, X. Pei, Q. Chen, P. Zhou, and D. Zhao, "A fast method for predicting the quasi-peak radiated EMI spectrum of power converters," in *Proc. IEEE Energy Convers. Congr. Expo.*, 2023, pp. 3415–3421, doi: 10.1109/ECCE53617.2023.10362668.
[40] A. Volke and M. Hornkamp, "IGBT modules: Technologies, driver and application," Infineon Technologies AG, Neubiberg, Germany, 2017.
[41] S. M. Sze and M. K. Lee, *Physics of Semiconductor Devices*, 4th ed. Hoboken, NJ, USA: Wiley, 2021.
[42] X. Yang, M. Xu, Q. Li, Z. Wang, and M. He, "Analytical method for RC snubber optimization design to eliminate switching oscillations of SiC MOSFET," *IEEE Trans. Power Electron.*, vol. 37, no. 4, pp. 4672–4684, Apr. 2022, doi: 10.1109/TPEL.2021.3127516.
[43] Denoising - MATLAB and Simulink, MathWorks, 2025. [Online]. Available: https://ww2.mathworks.cn/help/wavelet/denoising.html
[44] The MathWorks, Inc., "Curve fitter," MATLAB Documentation, 2025. [Online]. Available: https://www.mathworks.com/help/curvefit/curvefitter-app.html
[45] Mitsubishi Electric, "IGBT-MODULE-STD T/T1 series with 7th generation IGBT," 2025. [Online]. Available: https://www.mitsubishielectric.com/semiconductors/powerdevices/products/power-module/igbt-module-std/
[46] MathWorks, "ode45 - Solve nonstiff differential equations — Medium order method," MATLAB Documentation, 2024. [Online]. Available: https://www.mathworks.com/help/matlab/ref/ode45.html